ADVANCED MATERIALS
www.advmat.de

Reversible Structural Evolution of Metal-Nitrogen-Doped Carbon Catalysts During CO_2 Electroreduction: An Operando X-ray Absorption Spectroscopy Study

Dorottya Hursán, Janis Timoshenko, Eduardo Ortega, Hyo Sang Jeon, Martina Rüscher, Antonia Herzog, Clara Rettenmaier, See Wee Chee, Andrea Martini, David Koshy, and Beatriz Roldán Cuenya**

Electrochemical CO_2 reduction (CO_2RR) is a rising technology, aiming to reduce the energy sector dependence on fossil fuels and to produce carbon-neutral raw materials. Metal-nitrogen-doped carbons (M-N-C) are emerging, cost-effective catalysts for this reaction; however, their long-term stability is a major issue. To overcome this, understanding their structural evolution is crucial, requiring systematic in-depth *operando* studies. Here a series of M-N-C catalysts (M = Fe, Sn, Cu, Co, Ni, Zn) is investigated using *operando* X-ray absorption spectroscopy. It is found that the Fe-N-C and Sn-N-C are prone to oxide clusters formation even before CO_2RR. In contrast, the respective metal cations are singly dispersed in the as-prepared Cu-N-C, Co-N-C, Ni-N-C, and (Zn)-N-C. During CO_2RR, metallic clusters/nanoparticles reversibly formed in all catalysts, except for the Ni-N-C. This phenomenon, previously observed only in Cu-N-C, thus is ubiquitous in M-N-C catalysts. The competition between M-O and M-N interactions is an important factor determining the mobility of metal species in M-N-C. Specifically, the strong interaction between the Ni centers and the N-functional groups of the carbon support results in higher stability of the Ni single-sites, leading to the excellent performance of Ni-N-C in the CO_2 to CO conversion, in comparison to other transition metals.

1. Introduction

Electrochemical CO_2 reduction (CO_2RR) is a promising way to store the intermittent renewable energy in the form of chemical bonds and mitigate the atmospheric CO_2 at the same time.[1,2] The viability of this process depends on the development of efficient and *low-cost* catalyst materials,[3] as well as electrolyzer designs that operate at high current densities.[4] From the perspective of the catalysts, metal-based materials are by far the most studied CO_2RR systems.[3,5–7] Industrially-relevant current densities together with high selectivity have been recently reached for CO_2 conversion to CO and ethylene on silver- and copper-based catalysts, respectively.[8–10] To reduce the use of (precious) metal resources and to achieve maximum atom utilization, however, single atom catalysts (SACs) are an emerging new direction in catalysis science.[6,7,11] Metal-nitrogen-doped carbons (M-N-C) are a popular class of this family, first employed in the oxygen-reduction reaction,[12–14] but now widely used in several other electrochemical reactions too.[3,15–17] In these materials the metal centers are usually coordinated with the N, O, or C atoms of the support, leading to atomic dispersion of the metal with low-coordination and unique electronic structure. The metal-site coordination bears similarity to molecular complexes, however, they cannot be simply treated as "heterogenized" molecular catalysts.[15] On the contrary, they exhibit fundamentally distinct activity and selectivity from both molecular complexes and metallic (bulk or nanoparticulate) catalysts.

Depending on the nature of the metal-site and their coordination environment, M-N-C materials were demonstrated to be promising catalysts for the CO_2RR in recent years.[14,17–19] Ni-N-C and Fe-N-C are by far the most studied members of this family, showing high selectivity (>80% Faradaic efficiency, FE) toward CO.[20–24] While Fe-N-C demonstrates lower onset potential for CO formation, Ni-N-C allows higher current density and better selectivity at larger overpotentials.[14,19,25] Accordingly, Ni-N-C performs better when testing under high-current density (flow-cell) conditions.[20,22,23] On the other hand, for the Fe-N-C an intriguing ability to produce modest amounts of C_1 products beyond CO was reported.[26] Nonetheless, Ni-N-C is a unique

D. Hursán, J. Timoshenko, E. Ortega, H. S. Jeon, M. Rüscher, A. Herzog, C. Rettenmaier, S. W. Chee, A. Martini, D. Koshy, B. Roldán Cuenya
Department of Interface Science
Fritz-Haber Institute of the Max Planck Society
Faradayweg 4-6, 14195 Berlin, Germany
E-mail: janis@fhi-berlin.mpg.de; roldan@fhi-berlin.mpg.de

The ORCID identification number(s) for the author(s) of this article can be found under https://doi.org/10.1002/adma.202307809

DOI: 10.1002/adma.202307809

catalyst for CO_2RR, being able to largely suppress the parasitic HER, allowing for close to 100% FE for CO. This is attributed to the weak binding of H* to the active sites.[27] Since the first report on Ni-N-C for CO_2RR,[28] a large number of studies aimed at identifying the structure of the active center. Most works pointed out the crucial role of Ni-N_x motifs,[29,30,31] however, their evolution under CO_2RR conditions is not yet clearly understood, due to the limited number of *operando* studies available.

Whereas there is a relatively good agreement in the literature for Ni-N-C and Fe-N-C materials in terms of catalytic performance, the reports on other metal centers, such as Co and Cu are rather diverse. On Co-N-C the main CO_2RR product is also CO, but its FE varies in a wide range (from ≈20% to 95%) between different studies.[14,19,32,33] This can be attributed to different coordination environments around the metal center,[32,33] the presence of metallic particles in addition to single atoms[14] and variations in the carbon structure and morphology.[34] Note that the N-dopants are also active sites for CO formation,[35] which complicates the establishment of structure–performance correlations. The discrepancy is even more noticeable in the case of Cu-N-C. Several studies reported that the parasitic hydrogen evolution reaction (HER) dominated over CO_2RR for these catalysts.[14,17,36,37] Nonetheless, more recently high selectivities for CO,[38,39] CH_4,[40] CH_3OH[41] or even for C_{2+} products[42–44] were reported. The formation of C_{2+} products on singly dispersed metal sites is rather surprising as it was demonstrated before that reducing the size of Cu nanoparticles down to 2 nm suppressed the ethylene Faradaic efficiency to zero.[45] Through *operando* X-ray absorption spectroscopy (XAS) measurements, an intriguing phenomena was observed.[43,44,46,47] The Cu single sites present in the *as prepared* state of the Cu-N-C catalysts transformed into small clusters under CO_2RR conditions. Surprisingly, the clusters seemingly redispersed to single atoms, when they were exposed to air or an oxidizing potential after the reaction. This phenomena was first demonstrated on a catalyst with Cu-N_4 sites, producing ethanol with an impressive 40% Faradaic efficiency.[47]

In another work, the initial CuN_2Cl_2 sites transformed into Cu clusters with sizes around 1 nm and the FE for hydrocarbons (C_2H_4 + CH_4) reached as high as 81.3%.[44] An activation behavior was also observed in the latter work, i.e., the FE for CO_2RR products gradually increased, while that of HER decreased in time. The activation time was dependent on the metal-content, namely, catalysts with higher Cu content needed shorter time to reach a stable FE, possibly suggesting that Cu clusters grow in time. The Cu cluster formation during CO_2RR was also observed on molecular Cu complexes. Interestingly, the reversibility of the process depended on the type of ligand employed.[48] Inspired by the aforementioned works, catalysts intentionally containing Cu-clusters or small nanoparticles in a doped carbon matrix were also tested in the CO_2RR[43] and the CO reduction reaction (CORR)[37] showing high ethylene and ethanol selectivity. Nevertheless, the precatalyst (Cu cluster versus single atoms) had a determining role on the product selectivity.[43] These findings suggest that the real active sites for hydrocarbon and C_{2+} product formation on singly dispersed Cu-N-C catalysts are the metallic clusters formed during operation rather than the single metal sites.[46] This also highlights the importance of *operando* studies for investigations of M-N-C catalysts,[49] because relying exclusively on ex situ measurements may lead to false conclusions about the actual active sites, as was done in prior works when M-N-C samples were compared before and after reaction exclusively based on ex situ spectroscopy data.

To the best of our knowledge, the reversible cluster formation on single-atomic M-N-C materials has only been studied on Cu-centers so far. Furthermore, only a few *operando* investigations have targeted the systematic comparison of the behavior of different M-N-Cs under reaction conditions.[36,50] In two recent works, a family of M-N-C catalysts containing Mn-, Fe-, Co-, Ni- and Cu-sites,[36] as well as a set of small oxide clusters (Mn, Fe, Co, Ni and Cu) supported on N-doped carbon[50] were studied in CO_2RR and a volcano-like trend was identified between the activity toward CO formation and the atomic number of the transition metal. For M-N-C catalysts, the shifts observed in the X-ray absorption edge were interpreted as evidences of reversible lowering of the oxidation state of the metal sites.[36] For oxide clusters on N-doped carbon, the same authors interpreted the obtained *operando* extended X-ray absorption fine structure (EXAFS) data as an evidence of the presence of (hydr-)oxide clusters that show surprising resistance toward reduction under CO_2RR conditions.[50]

Our recent work, focusing on the mechanistic understanding of a single atomic Ni-N-C catalyst during CO_2RR, calls for caution when deciphering X-ray absorption near-edge structure (XANES) and EXAFS data from these catalysts.[31] The local structure around the metal site of M-N-C catalysts can be very complex, involving M-N, M-O, M-C, M-M bonds, interactions with adsorbates, and coexisting metal species with different environment and in different oxidation states, and thus, resulting in complex, broad distribution of different bond lengths and significant changes in the shapes of the XANES features. Furthermore, the presence of unique structural motifs in M-N-C catalysts, without analogues among bulk-like standard materials, poses a significant challenge for XAS data interpretation and often confuses the XANES and EXAFS data analysis, especially if it is not based on spectra modeling and if the XANES and EXAFS parts of XAS spectra are not considered together. For example, a key observation from our prior work[31] is that even minor changes in the local environment around the metal site (including the interaction between the metal and CO adsorbates) can result in dramatic changes in the XANES spectra, which can be misinterpreted as an evidence of the formation of a new species. As a result, considering that *operando* XAS is one of the few techniques that is able to provide insight into the working state of M-N-C catalysts under realistic electrochemical conditions, more in depth studies are needed for this promising class of catalysts to understand which species contribute to the catalytic functionality. Even for a well studied system such as Fe-N-C, the debate continues regarding the active state of the catalyst, with different authors suggesting Fe(III),[20] Fe(II)[36] and even Fe(I) species[51] as the active sites for CO_2RR. Moreover, appearance of Fe(0) species was also reported in an Ar-saturated electrolyte.[52] For other M-N-C materials the understanding of their working state is even further from being complete, since the number of existing reports on their *operando* transformations is limited. One study on Co-N-C reports the lack of any changes in the environment of singly dispersed Co sites,[36] whereas another work shows subtle changes in the Co K-edge XANES that led the authors to the somewhat surprising suggestion that Co valence might increase under reducing CO_2RR conditions.[33] For Sn-N-C, one recent operando

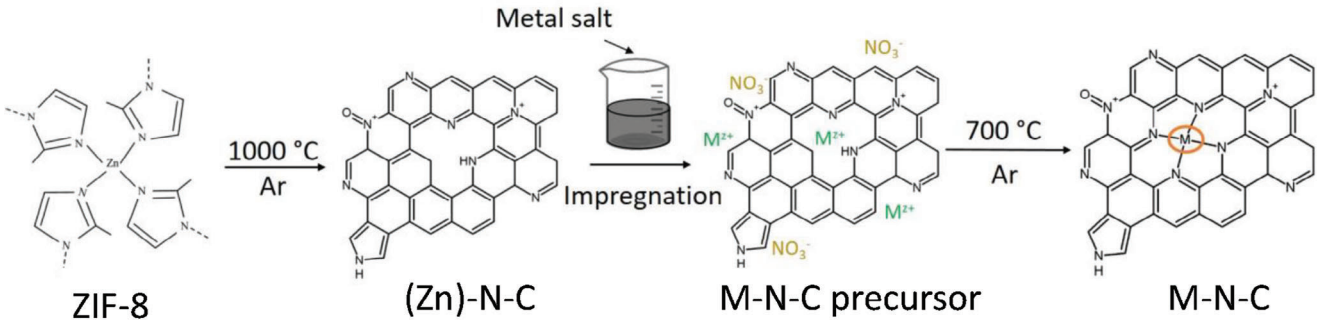

Scheme 1. Schematic of the catalyst synthesis.

XAS and Mössbauer spectroscopy study suggested[53] that the minor spectroscopic changes observed can be attributed to the interactions between singly dispersed Sn and O and CO_2 adsorbates. Furthermore, one popular approach for the synthesis of M-N-C catalysts relies on pyrolysis of Zn-containing metalorganic framework precursor.[54] As a result, many of the M-N-C catalysts have a significant contribution of Zn species, which also needs to be considered when interpreting structure-properties relationships in these catalysts.[7,36]

Motivated by the aforementioned findings and the lack of consensus in the literature about the working state of the M-N-C catalysts, we carried out here a detailed and systematic *operando* comparison of different M-N-C catalysts during CO_2RR and applied advanced data analysis methods to gain insight into the dynamic evolution of these materials under different chemical environments and under potential control. To this end, we synthesized a set of M-N-C catalysts differing in the nature of the metal center (Fe, Co, Cu, Sn, and Ni) and performed *operando* X-ray absorption (XAS) measurements during CO_2RR. Measurements for the bare (Zn)-N-C catalyst, containing residual Zn species, but without additional metal were also performed. The comprehensive analysis of the XANES and EXAFS spectra, complemented with detailed electron microscopic imaging gave insights into the real active sites of these materials, and allowed us to establish a link between the nature of the metal center and the observed catalytic functionality. A particular attention in this study was devoted to the phenomenon of reversible cluster formation from single metal site pre-catalysts. We found that this process is not unique for Cu-N-C catalysts, but, to lesser extent, can be observed in other M-N-Cs, most notably, for Co and Zn sites. On the other hand, for Ni-N-C our detailed XANES and EXAFS analysis confirms the lack of metallic clusters. The exceptional stability of Ni-N-C catalysts correlates with its excellent CO_2RR activity and CO selectivity, which we attribute to the strong interaction between Ni species and N-functional groups in the carbon support.

2. Results and Discussions

2.1. Ex Situ Morphological and Chemical Characterization

We synthesized the M-N-C catalysts by an impregnation-calcination method, starting from a zeolitic imidazolate framework (ZIF-8) precursor[54] as shown in **Scheme 1** and described in details in the Experimental Section. First, we characterized the catalysts by powder X-ray diffraction (XRD) (Figure S1, Supporting Information). The obtained diffractograms are typical for an amorphous carbon containing graphitic domains. The two broad peaks at around 25.5° and 43.4° are related to the (002) and (101) planes of graphite. We could not observe any reflections related to crystalline phases. Since small (<3 nm) highly disordered nanoparticles – especially when present in low concentration – might not give an XRD signal, the presence of such particles cannot be fully ruled out by XRD. Therefore, we carefully analyzed the as-prepared M-N-C samples by electron microscopy.

Figure 1 and Figures S2–S4 (Supporting Information) present a set of scanning transmission electron microscopy (STEM) images for each of the investigated catalysts. The low magnification STEM images show that the (Zn)-N-C support preserved the typical rhombic dodecahedron morphology of ZIF-8,[55] with a projected particle diameter of 55 ± 8 nm (Figure 1 and Figure S3, Supporting Information). The distinctive hexagonal edges of the (Zn)-N-C structure (Figure S3, Supporting Information) appear rounded in the case of Cu-N-C and Sn-N-C (Figure 1A) presumably due to the extra acid washing performed. In contrast, no regular shape or arrangement could be distinguished in the case of Fe-N-C. Furthermore, in this pristine sample we observed iron oxide nanoparticles with a wide size distribution, i.e., from 1 nm clusters to 20 nm aggregates (average: 8 nm, Figure S4, Supporting Information), despite the multiple acid-washing steps. The structures of this type were not present in any of the other samples. It was reported in the literature that it is challenging to obtain single-atomic Fe-N-C catalysts by such a wet-impregnation method.[56] This finding is supported by our present work too, as for the other metals the synthesis resulted in materials without visible metallic or oxide particles. To emphasize that this one sample differs significantly from the other catalysts, we hereinafter denote this sample as Fe-N-C_{cryst}.

From the high-resolution STEM (HR-STEM) images in Figure 1A (bottom row) it is possible to distinguish not only the amorphous carbon structure of the materials but also the presence of metallic single atoms in the carbon matrix. These single atoms are most apparent in the case of Sn-N-C, as tin has the highest atomic number among the studied metals, thus the contrast between Sn and C is the highest. In the case of Fe-N-C_{cryst}, single-atoms are also present (either Fe or Zn) in addition to the observed iron oxide nanoparticles. Energy-dispersive X-ray spectroscopy (EDS) mapping (Figure S5, Supporting Information) revealed the homogenous distribution of C, N, and Zn, as well as of the respective metal atoms in each catalyst, further

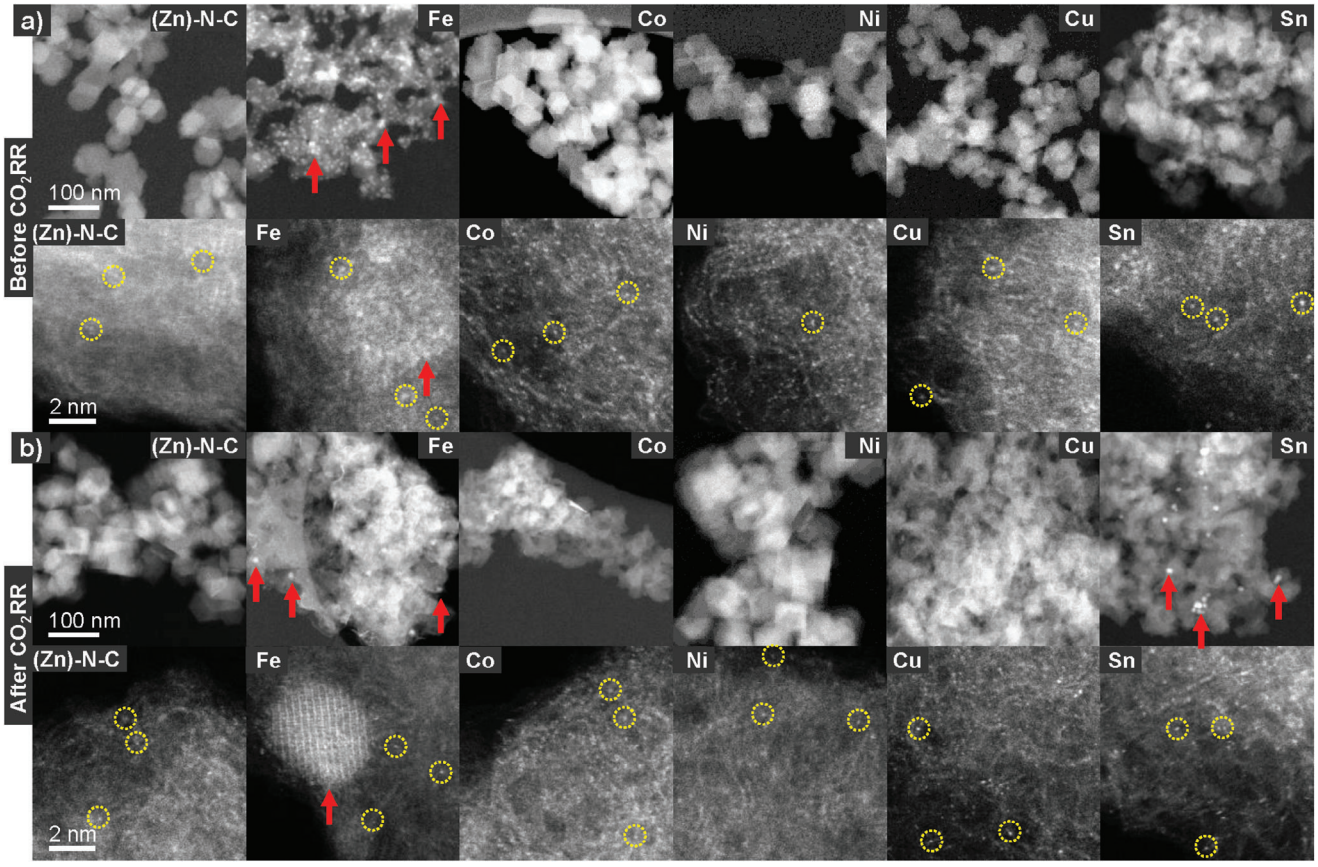

Figure 1. High angle annular dark-field scanning transmission electron microscopy (HAADF-STEM) images of the metal-nitrogen-doped carbon (M-N-C) catalysts in the as prepared state a) and after performing CO_2RR at −1.15 V for 80 min b). Low magnification (top) images show the morphological features of the M-N-C nanostructures and the presence of nanoparticles/aggregates (marked with red arrows). High resolution HR-STEM images (bottom) illustrate the disordered structure of the carbon framework and highlight the single atom doping of the added metals (yellow circles) as well as presence of small clusters and nanoparticles.

confirming that no agglomeration of the metal sites happened during synthesis (except for Fe-N-C_{cryst}).

We also employed TEM after performing CO_2RR on the M-N-C electrodes to reveal how the morphology of the catalysts and the dispersion of metal sites changed after the reaction (Figure 1B). Ni-N-C and Cu-N-C remained mostly unchanged after CO_2RR at −1.15 V. We could not observe nanoparticle formation for these catalysts, while the single metal sites were still present in the carbon matrix. We emphasize here that, in the light of previous reports demonstrating the reversible formation of Cu clusters in Cu-N-C catalysts,[43,44,47,50] this observation cannot be used to claim that no clusters were present during CO_2RR. For Co-N-C we observed the formation of some needle-like particles after CO_2RR (Figure S6, Supporting Information). EDS elemental mapping revealed, however, that these were Zn-rich agglomerates, while Co remained dispersed in the material. The atomically-resolved STEM images (Figure 1B bottom row) confirmed the presence of single atomic metal sites after reaction too. In the case of Sn-N-C, small nanoparticles (< 5 nm average particle size) were commonly present in the carbon matrix after reaction (see also Figure S7 in the Supporting Information) besides the singly dispersed metals. The formation of Sn/SnO_x nanoparticles was already observed at −0.55 V (Figure S8, Supporting Information), with slightly larger average particle size compared to the case when the electrolysis was performed at −1.15 V (4.9 vs 2.8 nm, Figure S10, Supporting Information).

Finally, the structure of the Fe-N-C_{cryst} after reaction looked alike to the *as prepared* catalyst, with the crystalline nanoparticles still present in the material. The size distribution of the nanoparticles after reaction was very similar to the *as prepared* state, the average particle size increased only by ~0.6 nm after CO_2RR (Figure S10, Supporting Information). For the bare (Zn)-N-C the images after reaction (Figure S9, Supporting Information) showed the presence of some ZnO nanoparticles.

We studied the surface chemical composition and speciation of the catalysts by X-ray photoelectron spectroscopy (XPS). During the survey scans (Figure S11, Supporting Information) the presence of C, N, O, Zn and the main metal atoms (Fe, Sn, Cu, Ni, Co) was detected, confirming the nitrogen- and metal doping of the carbon structure. The relative amounts of C, N and O atoms were similar in each catalyst, corresponding to 87.3–91% C, 4.4–5.8% N, and 4–7.8% O (Table S1, Supporting Information). The metal contents (including Zn for all samples) were below 0.5 at % in each case. We also determined the bulk metal-contents by ICP-MS (Table S2, Supporting Information), which showed good agreement with the XPS results. Only in the case

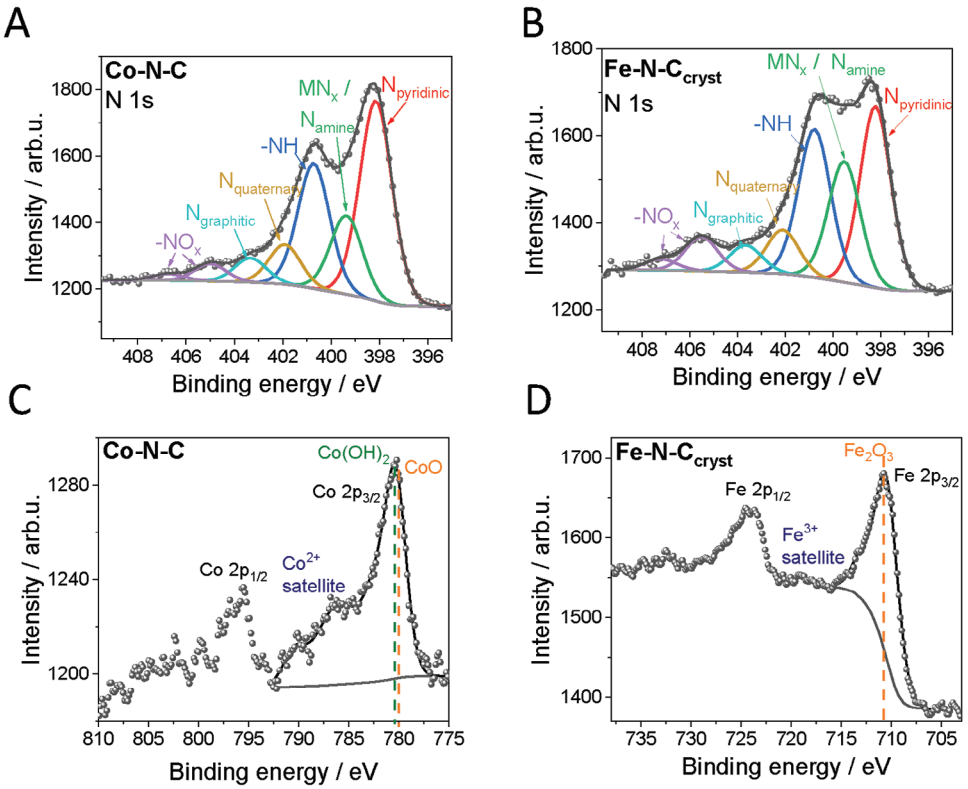

Figure 2. High resolution X-ray photoelectron spectra of Co-N-C A,C) and Fe-N-C_{cryst} B,D). The N 1s A,B) and the respective metal 2p C,D) regions are presented. For the metal regions the main XPS lines of reference compounds taken from the literature are also shown.[57,58] Spectra for the other catalysts are shown in Figures S12 and S13 (Supporting Information).

of Fe-N-C_{cryst} we observed significantly lower Zn-concentration based on the XPS measurement. This is probably because the multiple acid-washing (employed to try to remove the crystalline the Fe species) also removed Zn-species from the surface, however, they remained intact in the bulk of the material.

The high resolution N 1s and respective metal regions (**Figure 2**; Figures S12 and S13, Supporting Information) were also recorded. In accordance with previous reports on similar materials, we fitted the N 1s spectra with the following components:[59–64] pyridinic N at 398.2 eV, metal coordinated N / amine N at 399.3 eV, N-H at 400.7 eV, quaternary N at 402.0 eV, graphitic N at 403.3 eV and finally oxidized N between 405 and 408 eV. For the more detailed assignment of the peaks, see the discussion below Figure S12 in the Supporting Information. Overall, we found similar N-speciation for all studied catalysts (Table S3, Supporting Information), being pyridinic N the main component, followed by the –NH and the M–N_x / amine species. We note that Cu-N-C and Fe-N-C_{cryst} were richer in metal-coordinated N-moieties, as compared to the other catalysts, which may indicate stronger interaction between the metals and the N-sites of the carbon. Furthermore, the Cu-N-C, Sn-N-C, and Fe-N-C_{cryst} samples contained around 1.5 to 2-times higher amounts of –NO_x, than Ni-N-C, Co-N-C, and (Zn)-N-C (plain support). The reason for this is the presence of residual NO_3^- ions on the surface resulting from the additional acid-treatment employed for these samples.

The analysis of the respective metal XPS regions (Figure 2 and Figure S13, Supporting Information) unveiled information about the oxidation state of the metal centers. Because of the low metal loading (hence weak signal intensity), accurate deconvolution employing the typical multiplet fitting features of metal-oxides and hydroxides could not be performed. Instead, we focused on the position of the main peak and the presence/absence of satellite features.[14] The analysis of the metal regions revealed that the metal sites are mainly in an oxidized state, as expected for SACs. In the case of Co-N-C the main peak is located at 780.3eV, with a significant satellite structure (42% of the main line), resembling the spectra of CoO or $Co(OH)_2$ (+2 oxidation state).[57] Note that the main peak of Co-porphyrine is also located at 780.3 eV, however, with a much weaker satellite structure.[58] The spectrum of Cu-N-C shows that the oxidation state of copper is mainly +2 (main peak at 934.6 eV), though there is a minor contribution from Cu^0 or Cu^+ species.[65] In the case of Ni-N-C the main peak is centered at 855.3 eV, which is in accordance with either a $Ni(OH)_2$ or a Ni-porphyrine-like structure.[57,58] The tin in Sn-N-C is in a cationic form too (main peak at 486.6 eV), however, we cannot tell unambiguously, whether it is Sn^{2+}or Sn^{4+}, as the binding energies of these two species are very close to each other (reported values lie between 486.0 and 487.0 eV for SnO, and between 486.6 and 487.3 e V for SnO_2).[66,67] Finally, there is a broad peak at 710.7 eV in the case of Fe-N-C_{cryst}, with a weak satellite feature at 719.2 eV, which is typical of Fe_2O_3.[57]

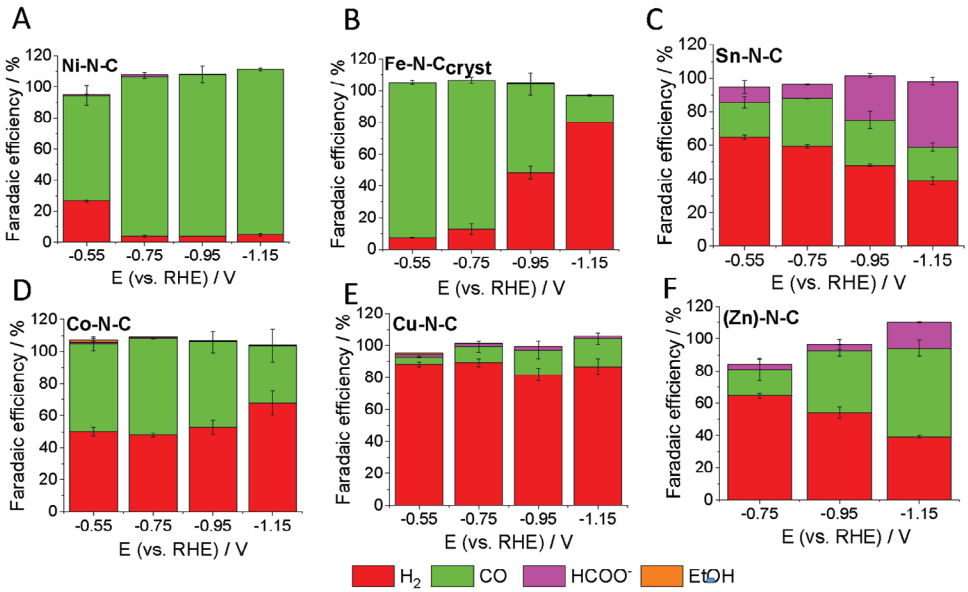

Figure 3. Potential-dependent CO_2RR selectivity of M-N-C electrodes. Measurements were performed in an H-type cell using a CO_2-saturated 0.1 M $KHCO_3$ electrolyte. The data represent the selectivity in the 80th minute of the electrolysis. Error bars give the standard deviation of the data measured on at least two individual samples. Figure 3A was reproduced under terms of the CC-BY license.[31] Copyright 2023, The Authors, published by ACS.

2.2. CO_2 Reduction Performance

The CO_2 reduction performance of the catalysts was studied in an H-cell configuration in a CO_2-saturated 0.1 M $KHCO_3$ solution. First, linear sweep voltammograms were recorded for a quick comparison of onset potentials and current densities (Figure S16, Supporting Information). The least negative onset potential was observed for Fe-N-C_{crys} and Co-N-C, followed by Ni-N-C, Cu-N-C, Sn-N-C and finally the bare (Zn)-N-C. The current densities followed the same trend in the studied potential window. As a next step, we studied the selectivity of the CO_2RR by analyzing the products in the gas- and liquid phase at different potentials between −0.55 V_{RHE} and −1.15 V_{RHE} (**Figure 3**). We note that the slight deviation of the sum of the faradaic efficiency (FE) values from 100% results from the limitations of our analytical technique and electrolysis setup, which is discussed in the experimental section. CO and H_2 were the main products in the gas-phase for all catalysts, while formate was detected in the largest amount in the liquid-phase. In the liquid-phase trace amounts of methanol and ethanol were also formed on certain catalysts (Table S4, Supporting Information). Interestingly, not only Cu-N-C produced these liquid products, but Co-N-C and Fe-N-C also showed minor activity toward them. Methanol and methane formation on Fe-N-C was reported previously, and based on DFT calculation was attributed to the relatively strong binding of CO* to the Fe-N_4-C sites.[14,52] Because of the isolated active site structure of these catalysts (i.e., difficulty of H* and CO* coadsorption), however, the reaction rate toward these products is limited. Ni-N-C and Fe-N-C_{cryst} showed the highest CO-selectivity ($FE_{CO,max}$> 90%), in accordance with previous literature reports.[14,36] At the lowest overpotential (−0.55 V_{RHE}), the FE_{CO} of Fe-N-C_{cryst} exceeded that of Ni-N-C, however, starting from −0.95 V_{RHE}, the HER on Fe-N-C_{cryst} greatly increased. In contrast, Ni-N-C reached its maximum FE_{CO} at more negative potentials (≤ −0.75 V_{RHE}). The drastic decrease of FE_{CO} and the concomitant increase in HER rate on Fe-N-C_{cryst} below −0.95 V_{RHE} (**Figure 4D**) can be attributed to the strong CO*-binding of single atomic Fe sites at large overpotentials impeding desorption of CO,[14] as well as to the presence of crystalline Fe phases starting to catalyze HER at these potentials.[68] As reported in a previous study, while a Fe-N-C catalyst containing single-atomic Fe-sites in the *as prepared* state produced CO with high selectivity, iron / iron-oxide particles in an N-doped carbon matrix formed mainly H_2. However, no *operando* data were reported to show how the Fe sites change during reaction.[68] Thus, although the identity of the active sites of Fe-N-C materials in CO_2RR is still not clear, the interaction between the Fe species and the N-sites of the carbon[50,69] as well as the size of any possible residual crystalline Fe clusters / nanoparticles seem to play a role. In the case of Co-N-C, FE_{CO} fluctuated around 50% between −0.55 and −0.95 V_{RHE} (with the rest being H_2), while at the most negative potential the FE for CO dropped to around 30%. For Sn-N-C, the overall selectivity for CO_2RR products increased with increasing overpotential. While CO was the main CO_2RR product at less negative potentials (at −0.55 V_{RHE}, 38% CO), formate started to dominate below −0.95 V_{RHE}, reaching 48% at −1.15 V. Cu-N-C was the least selective for CO_2RR products among the investigated catalysts, as more than 80% of the current was used for H_2 formation at all studied potentials. Finally, the (Zn)-N-C reference also showed activity in CO_2RR, yielding CO and formate. Its FE_{CO} reached 50% at −1.15 V_{RHE}, and formate was formed in non-negligible amounts (16% *FE*) too. The CO_2RR activity of (Zn)-N-C originates from both the N-species and the Zn-sites.[70,71] For this catalyst, however, the current density (Figure 4A) was greatly reduced compared to the metal-containing electrodes (3.5-times lower than for Cu-N-C and 7-times lower than for Co-N-C at −1.15 V_{RHE}).

The higher overall current densities for the M-N-C catalysts clearly demonstrate that the incorporated metal sites give extra

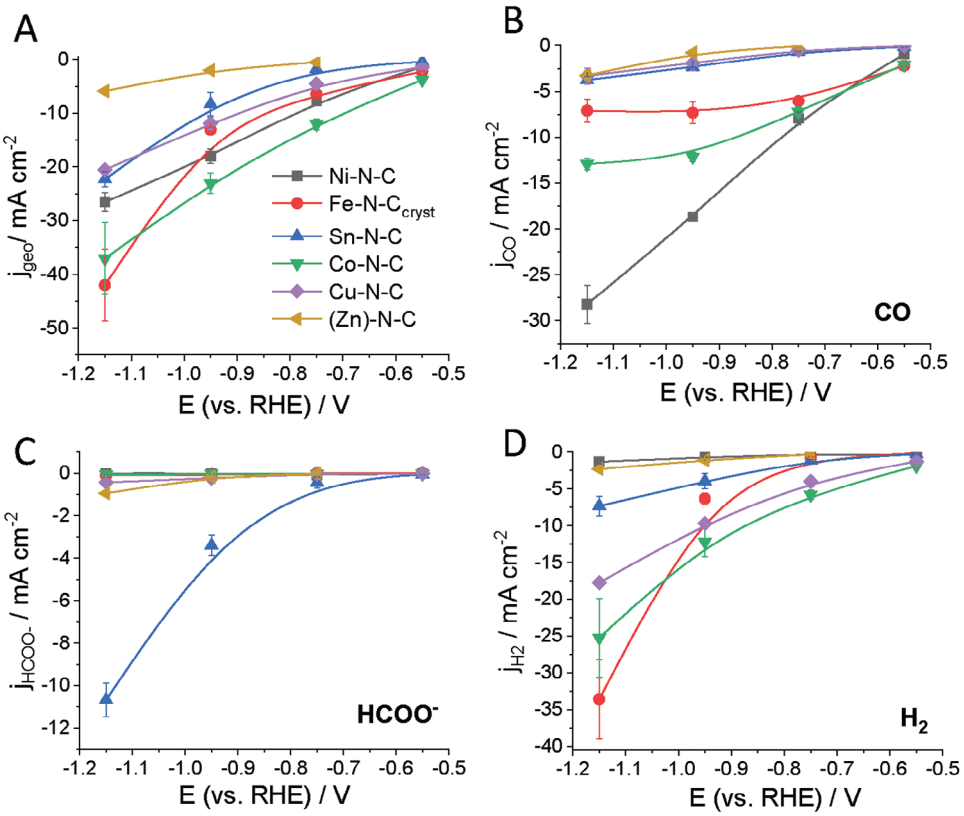

Figure 4. Total A) and partial B–D) current densities for CO and $HCOO^-$ and H_2 on the investigated catalysts normalized by the geometric surface area of the electrodes Data were measured in the 80th minute of the potentiostatic electrolysis in a CO_2-saturated 0.1 M $KHCO_3$ solution. Error bars give the standard deviation of the measurements repeated at least on two individual samples. Lines serve only as a guide for the eye.

catalytic activity to the (Zn)-N-doped carbon matrix. This was also true when we normalized the currents by the roughness factors (Figure S17, Supporting Information), proving that the observed catalytic differences arise from the distinct intrinsic activity of the metal (cation) sites, rather than the slightly varying electrochemical surface areas (Figure S15, Supporting Information). Therefore, the activity of the (Zn)-N-C can be regarded as a baseline and the activity difference between the respective M-N-C catalysts and (Zn)-N-C is attributed to the given metal cation site.

We also plotted the partial current densities for CO, H_2, and formate to compare the product formation rates on the different catalysts (Figure 4 and Figure S17, Supporting Information). From the roughness factor-normalized currents, it became clear that the Co sites are the most active both in H_2 and CO production. The CO-formation rate on Ni-N-C was very close to that of Co-N-C, however, Ni-N-C showed almost negligible HER (below that for (Zn-)N-C), confirming the excellent CO_2 to CO conversion performance of the single atomic Ni. Fe-N-C_{cryst} showed relatively high CO production rate too (especially below −0.75 V_{RHE}), significantly exceeding that of Sn-N-C and Cu-N-C. This trend is in a good agreement with a previous study reporting a volcano-trend between the CO formation activity and the atomic number of the transition metal.[36] In terms of formate production, only the Sn-sites showed significant activity, which was more than ten times higher (at −1.15 V_{RHE}) than that of the bare (Zn)-N-C. Overall, the selectivity trends for the studied M-N-C catalysts agreed well with previous literature reports on similar materials. This offered us a platform for a systematic *operando* XAS study to investigate the evolution of the active sites during CO_2RR.

2.3. Operando XAS Investigation

The evolution of the Fe, Co, Ni, Cu, Sn and Zn K-edge XANES spectra for Fe-N-C, Co-N-C, Ni-N-C, Cu-N-C, Sn-N-C, and (Zn)-N-C catalysts under CO_2RR conditions is shown in **Figure 5** and Figure S18 (Supporting Information). Corresponding EXAFS spectra for the *as prepared* catalysts and catalysts in their final state under CO_2RR conditions at −1.15V_{RHE} are shown in **Figure 6**. EXAFS data collected at less negative potentials, as well as after the experiment and exposure to air are shown in Figure S19 (Supporting Information). Corresponding Fourier-transformed (FT) EXAFS spectra are shown in Figures S20–S22 (Supporting Information). These plots of XAS data in energy-space, *k*-space and *R*-space highlight different aspects of the analyzed spectra, and help us to identify better the main structural motifs. Furthermore, in **Figure 7** and Figure S23 (Supporting Information) we show the results of short time Fourier transformation (STFT) of the EXAFS spectra. STFT is a signal processing technique that is similar to wavelet transform[72,73] (WT, commonly used for the interpretation of EXAFS spectra of single atom catalysts). Both STFT and WT allow one to represent the EXAFS spectrum in *k*- and

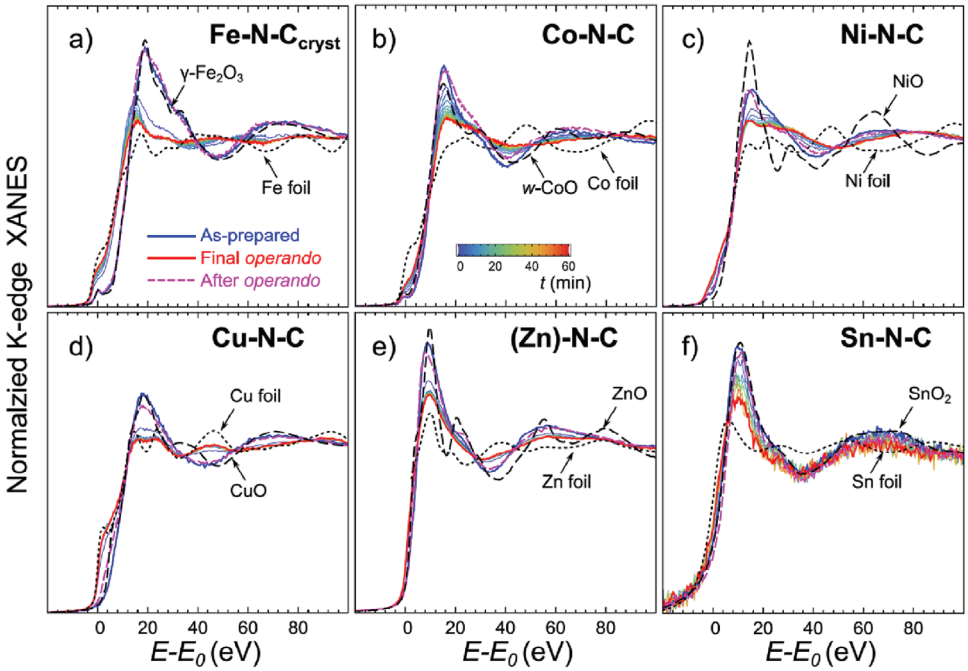

Figure 5. K-edge XANES for a) Fe in Fe-N-C$_{cryst}$, b) Co in Co-N-C, c) Ni in Ni-N-C, d) Cu in Cu-N-C, e) Zn in (Zn)-N-C, f) Sn in Sn-N-C, and their evolution during 1 h of CO_2RR at −1.15 V_{RHE}. Spectra for the same samples after reaction and exposure to air are also shown, as well as reference spectra for the respective metal foils and oxides.

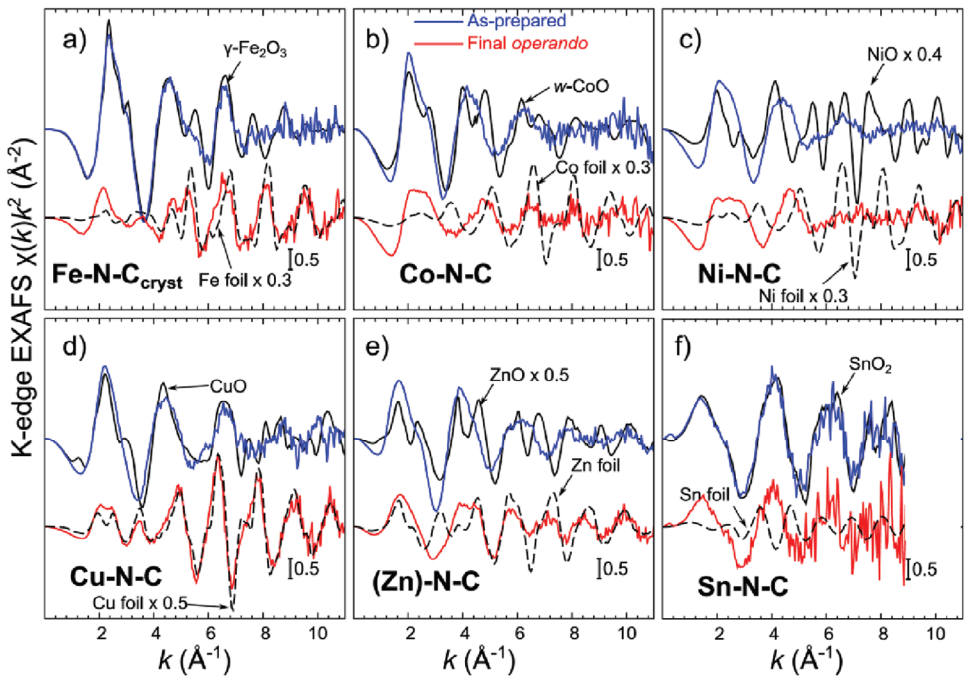

Figure 6. K-edge EXAFS for a) Fe in Fe-N-C$_{cryst}$, b) Co K-edge EXAFS for Co-N-C), c) Ni in Ni-N-C, d) Cu K-edge EXAFS for Cu-N-C, e) Zn K-edge EXAFS for (Zn)-N-C, f), Sn K-edge EXAFS for Sn-N-C f). Spectra for the *as prepared* samples (blue), and samples during CO_2RR at −1.15 V_{RHE} (red) are shown. Reference spectra for respective metal foils and oxides are also plotted, scaled, as indicated in the plots, for better visibility. Spectra are shifted vertically for clarity.

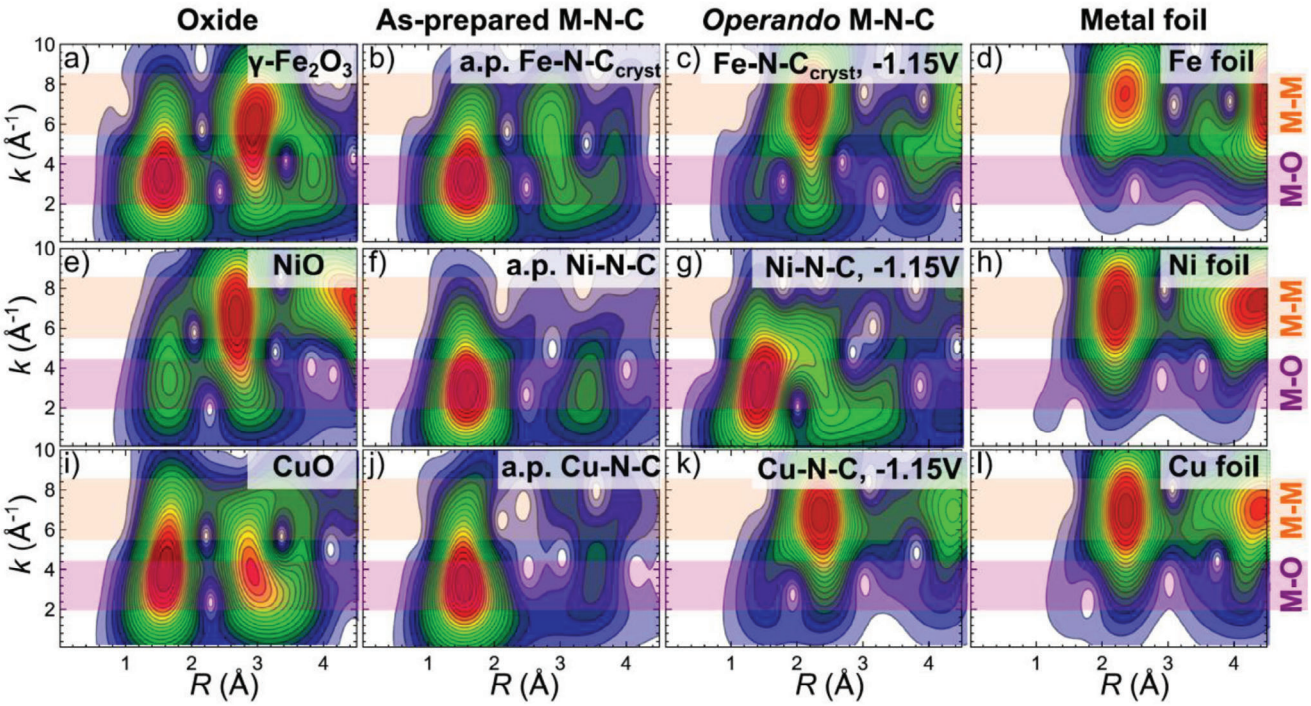

Figure 7. Short-time Fourier-transforms of Fe K-edge EXAFS for Fe-N-C_{cryst} and reference materials a–d), Ni K-edge EXAFS for Ni-N-C and reference materials e–h) and Cu K-edge EXAFS for Cu-N-C and reference materials i–l). Spectra for the as-prepared M-N-C samples b,f,j), and samples under CO_2RR at −1.15 V_{RHE} c,g,k) are shown. The color scales in different panels do not match.

R-spaces simultaneously, by showing where in *k*-space the spectral components with different *R*-values are localized. The mathematical details and the comparison of STFT and WT methods in given in Note S2 (Supporting Information).

Although our catalysts are based on different transition metals, one can note certain similarity between their XANES spectra and their evolution during and after CO_2RR (Figure 5). For all the *as prepared* catalysts, the position of the absorption edge matches well that of XANES spectra for reference oxides: γ-Fe_2O_3 in the case of the Fe-N-C_{cryst} catalyst, CoO in the case of Co-N-C, NiO in the case of Ni-N-C, CuO in the case of Cu-N-C, ZnO in the case of the (Zn)-N-C reference support, and SnO_2 in the case Sn-N-C. XANES spectra for the *as prepared* samples are also characterized by an intense white line feature. This suggests strong charge transfer from the metal atom to ligands and/or hybridization of metal *d*-states with *p*-states of ligands, resulting in intense dipole-allowed transitions of the s-electrons from the core levels to vacant *d*-states.[49] These observations allow us to conclude that the oxidation state of the metals in the *as prepared* state of the catalysts are as follows: +3 for Fe in Fe-N-C_{cryst}, +4 for Sn in Sn-N-C, and +2 for Cu, Ni, Co and Zn in Cu-N-C, Ni-N-C, Co-N-C, and (Zn)-N-C, respectively, in accordance with the XPS results. Under CO_2RR conditions, the intensity of the white line is strongly suppressed in all catalysts, suggesting strong changes in the local environment of the metal sites. Remarkably, in all cases these changes are reversible: after the reacted samples are exposed to air, the intensity of the white line and other XANES features becomes very similar to those in the as prepared samples. This makes imperative to rely on *operando* investigations for understanding the working state of this class of catalysts.

For the as-prepared samples, the post-edge region of XANES spectra is relatively featureless, suggesting the high structural disorder present in these samples. Meanwhile, the FT-EXAFS spectra in Figure S20 (Supporting Information) are dominated by a strong peak between ca. 1–2 Å (phase uncorrected), which we attribute to the bond between the metal M and some light backscattering atom (O, N or C). In general, for the as-prepared Fe-N-C_{cryst}, Co-N-C, Cu-N-C, and the Sn-N-C, and also for the Zn species in the as-prepared (Zn)-N-C there is good agreement between the shape of the main XANES features (Figure 5), EXAFS signal frequencies (Figure 6) and shapes, positions and intensities of the main FT-EXAFS peak (Figure S20, Supporting Information) with those in the respective reference oxide. This suggests similar first coordination shell environment for the as-prepared M-N-C catalysts and oxide references. In the case of the as-prepared Co-N-C catalyst, it is interesting to note that its XANES and EXAFS data match better the spectra for wurtzite-type CoO reference (*w*-CoO), rather than those of a more common rocksalt-type CoO (*rs*-CoO). This indicates that the local environment around the Co site in Co-N-C is more distorted than the octahedral environment of Co in *rs*-CoO. In all these cases, the agreement between XANES and EXAFS features for the as-prepared M-N-C catalysts and for the oxide reference suggests the presence of M-O bonds in the first coordination shell of metal sites in our M-N-C catalysts, rather than (just) M-N bonds: note that while nitrogen and oxygen have similar photoelectron scattering properties, the expected M-O and M-N bond lengths could differ noticeably.[31] And, indeed, the presence of axial M-O or M-OH bonds (coexisting with in-plane M-N bonds) is in agreement with recent reports

on the structure of Fe-N-C_{cryst}[52] and Sn-N-C[53] catalysts for CO_2RR and Co-N-C catalyst for CO_2 photoreduction.[74] For the as-prepared Ni-N-C, we observe the largest discrepancy between the XAS data for the catalyst and the corresponding reference oxide: the intensity of the XANES white line is lower than that of the NiO reference (Figure 5c), and, more importantly, the main FT-EXAFS peak is shifted to lower interatomic distances than that of the bulk NiO reference (Figure S20C, Supporting Information). For Ni-N-C, our recent work relying on ab-initio XANES simulations, machine learning methods and EXAFS modeling,[31] has shown that the spectra for the as-prepared Ni-N-C catalyst can be best described by an octahedral structural motif featuring four strong and short in-plane Ni-N bonds, and two longer axial Ni-O bonds. Thus, based on our result, the axial M-O bonds contribute to XAS data for all our investigated M-N-C materials.

In addition to the main FT-EXAFS peak, contributions of distant coordination shells to the EXAFS spectra of the as-prepared catalysts are also present, but these are typically much weaker. An important exception is the Fe-N-C_{cryst} catalyst, where strong FT-EXAFS peaks at ≈2.5 and 3.5 Å are observed, Figure S20A (Supporting Information). The positions of these additional peaks match the features in the FT-EXAFS spectrum of the γ-Fe_2O_3 reference. This observation, supported by a nearly perfect agreement of XANES (Figure 5A) and *k*-space EXAFS (Figure 6A) spectra for the as-prepared Fe-N-C_{cryst} and for γ-Fe_2O_3 reference, allows us to conclude with confidence that the majority of Fe in the as-prepared Fe-N-C_{cryst} forms oxide clusters, thus confirming the electron microscopy findings for this sample. We note that the relative intensity of distant shell peaks in Fe-N-C_{cryst} is lower than that in the bulk oxide reference, suggesting small particle sizes and/or their strongly disordered nature, which explains why these particles were not detected by XRD measurements. On the other hand, the reduced amplitude of the Fe_2O_3-like distant coordination shell contributions might also imply that the clusters of Fe_2O_3 coexist in our catalyst with some fraction of Fe species that have no such medium range order, namely, singly dispersed Fe^{3+} sites.

Understanding the weak features between the 3.0 and 4.0 Å in the FT-EXAFS spectra for the other as-prepared M-N-C catalysts requires more careful analysis. Here, the STFT analysis is very helpful (Figure 7; Figure S23, Supporting Information). By showing the location of different spectral components in *k*-space, STFT indicates whether certain spectral features are attributed to light backscatters or metallic neighbors. The former typically exhibit maxima of intensity at lower *k*-values (between 2 and 4 $Å^{-1}$), while the latter at higher *k*-values (between 6 and 7 $Å^{-1}$ for the first row transition metals, and even higher *k*-values for more heavy metals). For example, in the case of the Fe-N-C_{cryst} it is easy to see the similarity of STFT-EXAFS maps for the as-prepared catalyst and the γ-Fe_2O_3 reference, including the presence of a strong peak at *R* values of ≈3.0 Å and *k*-values of ≈6.0 $Å^{-1}$, which, thus, can be assigned to the second coordination shell Fe–Fe bond in an iron oxide structure (Figure 7A,B). Similarly, for the Sn-N-C catalyst STFT shows very conclusively that the two small FT-EXAFS peaks between 3.0 and 4.0 Å (Figure S20F, Supporting Information), have the same origin as those peaks in the FT-EXAFS spectrum for SnO_2. Indeed, the corresponding STFT maps for SnO_2 and the as-prepared Sn-N-C are, again, very similar (Figure S23I,J, Supporting Information), and both feature a strong peak at *R* values ≈3.5 Å and *k* values ≈8.0 $Å^{-1}$, which can be assigned with confidence to a Sn-Sn bond in the oxide structure. Thus, the STFT-EXAFS shows that the as-prepared Sn-N-C also contain oxide clusters, similarly as Fe-N-C_{cryst}. The reason that we did not see such clusters during the TEM imaging of Sn-N-C is their possible inhomogeneous distribution in the material. Interestingly, the situation is different for the other M-N-C catalysts. Indeed, the STFT-EXAFS maps for Co-N-C, Ni-N-C, Cu-N-C, and Zn species in (Zn)-N-C in the as-prepared state are all remarkably similar, and all show the presence of a STFT feature at *R* values ≈3–4 Å and at low *k*-values (2–3 $Å^{-1}$). The location of this feature in *k*-space suggests that it corresponds to the bond between a metal site and a light atom, rather than M–M bond in the second coordination shell of oxide or hydroxide. In our previous work on Ni-N-C,[31] using XANES simulations and EXAFS fitting using reverse Monte Carlo approach we have demonstrated that this feature is due to bond between the metal site and carbon support, and, thus, is a characteristic of singly dispersed metal species. Our current study thus expands this observation also to Co-N-C, Cu-N-C systems, and Zn species in (Zn)-N-C catalysts.

In agreement with the observations from XANES data under CO_2RR conditions, EXAFS spectra for all catalysts change strongly and, crucially, reversibly (Figure 6,7 and Figures S19–S23, Supporting Information). The most obvious changes were observed for the Cu-N-C and Fe-N-C_{cryst} catalysts (Figure 6A,D and Figure S20A,D, Supporting Information). The FT-EXAFS peak corresponding to the metal-ligand bond is suppressed, while new FT-EXAFS peaks develop at positions matching closely the positions of FT-EXAFS peaks in metallic Cu and Fe. We highlight here that not only we observe a new peak at ≈2 Å, corresponding to the first shell interatomic distance in the metallic phase, but also the shapes, positions and intensities of more distant peaks in the Cu-N-C and Fe-N-C_{cryst} catalysts match nicely those for the respective metal foils, suggesting the formation of fcc-type clusters in Cu-N-C, and of bcc-type metal clusters in Fe-N-C_{cryst} catalysts.

The changes in the local structure of other M-N-C catalysts are more subtle, and can be best seen in EXAFS data in *k*-space (Figure 6). One can see that also in the case of Co-N-C and Zn species in (Zn)-N-C during CO_2RR at −1.15 V_{RHE} the EXAFS spectrum at larger *k*-values is dominated by a sinusoidal signal with a frequency matching the frequency of the EXAFS signal for the respective metal foil. STFT-EXAFS maps (Figure 7, and Figure S23, Supporting Information) support this conclusion. Here, similarly as in the case of Fe-N-C_{cryst} and Cu-N-C, we observe an increase in the signal intensity in the two main regions where a contribution of metal-metal bonds is expected: at (*R*,*k*) values ≈(2.5 Å, 7.0 $Å^{-1}$) and ≈(4 Å, 7.0 $Å^{-1}$). It is not the case for Ni-N-C, where the EXAFS spectrum experiences significant changes during CO_2RR, but no signs of metal-metal bond formation is observed in the *k*-space EXAFS (Figure 6C) or STFT-EXAFS (Figure 7E–H). This reveals that the structural changes experienced by the Ni sites, are limited to the re-arrangement of bonds with light atoms. We note here that, overall, the trends in *operando* Ni K-edge EXAFS spectra are the same as observed in our previous work.[31] Namely, the observed changes in the Ni K-edge EXAFS are a result of the direct interactions between the

single Ni site and CO adsorbates under CO_2RR conditions, which result in a cleavage of the axial Ni-O bonds and their replacement with CO adsorbates, resulting also in a distortion of the Ni-N_4 structural motif. More details on this system can be found in ref.[31] Regarding the Sn-N-C system, visual examination of EXAFS data do not provide conclusive evidences about the formation of metal clusters (or lack of thereof). The poor signal-to-noise ratio in the *operando* EXAFS spectrum limits our ability to compare this spectrum directly with the *k*-space data for a metallic Sn foil (Figure 6F). Furthermore, we note that even bulk Sn metal displays a strongly distorted structure, resulting in a relatively weak EXAFS signal, which would be hard to identify in the noisy data. We note, nonetheless, that the amplitude of the Sn-O bond contribution in the Sn-N-C catalysts under CO_2RR conditions is reduced with respect to that in the *as prepared* sample (Figure 6F and Figure S20F, Supporting Information), followed by the appearance of smaller peaks at larger *R*-values in the FT-EXAFS spectra. The results of STFT-EXAFS analysis suggest that these spectral contributions are indeed localized at high *k*-values (Figure S23K, Supporting Information), where we expect to see the contribution of metallic Sn-Sn bonds. Nonetheless, since the high *k*-space region of our spectrum is also the one most affected by experimental noise, the conclusion about the possible presence of metallic Sn clusters should be made with caution. In any case, it seems that even if such metallic clusters are present in the working Sn-N-C catalyst, their structure differs strongly from the structure of common metallic tin phases, since FT-EXAFS and STFT-EXAFS spectra are quite different.

It is important also to highlight here that for Fe-N-C_{cryst}, Cu-N-C, Co-N-C, and (Zn)-N-C systems, where the formation of metallic clusters/nanoparticles under CO_2RR conditions is observed, the catalysts do not turn fully metallic (at least within 1 h of CO_2RR), and the contribution of metal bonds with light nearest neighbors is still present in all EXAFS spectra in all our catalysts. This suggests that a noticeable fraction of metal sites preserves their singly dispersed nature (or their cationic state), and, thus, the contribution of these species to the catalytic functionality cannot be ruled out. It is plausible that at least in the production of CO (e.g., for Fe-N-C_{cryst}), the minority single atom species available in these samples constitute the most active species, with the larger clusters formed being spectators. This would be in agreement with prior work in refs.[14,68] On the other side, for C-C coupling detected in systems like the Cu-N-C, the Cu clusters or nanoparticles formed during CO_2RR constitute the active species.[47]

Regarding the effect of the potential value applied during CO_2RR, we note that the evolution of all of our catalysts is qualitatively similar both at −0.55 and −1.15 V_{RHE} (Figures S18, S19, and S22, Supporting Information). In particular, the formation of metallic clusters in Fe-N-C_{cryst}, Cu-N-C catalysts is comparable at these two potentials. Similarly, the formation of metallic Zn clusters in (Zn)-N-C catalyst is comparable at –0.75 V_{RHE} and –1.15 $V_{RHE.}$ We note, nonetheless, that in the case of Co-N-C and Sn-N-C, the formation of metallic clusters is less pronounced at less negative potential. Furthermore, for Ni-N-C, the *operando* XANES and EXAFS data collected at –0.55 V_{RHE} are in between the spectra for the as-prepared catalyst and for the catalyst at –1.15 V_{RHE}. Supported by our previous work,[31] we conclude that at less negative potential the replacement of axial oxygen ligands by CO adsorbates is likely to be incomplete in the Ni-N-C catalyst, and some Ni-O bonds are still preserved.

For a more quantitative assessment of the structural changes experienced by working M-N-C catalysts, we employ linear combination analysis (LCA) of XANES spectra and non-linear least-square fitting of EXAFS data. For this class of materials, LCA-XANES should be applied with caution, since we expect that the structures of the catalysts differ strongly from the structure of common bulk references. LCA-XANES results thus should always be supported by other methods, such as EXAFS analysis. Nonetheless, we have found that for Fe-N-C_{cryst}, Cu-N-C, Sn-N-C and (Zn)-N-C, LCA-XANES provides meaningful results (Figure S25 and Table S5, Supporting Information).

The case of Zn species in (Zn)-N-C is the simplest. Here, the *operando* Zn K-edge XANES can be very well described as linear combinations of XANES spectra for the as-prepared sample and for the Zn foil. Moreover, even Zn K-edge EXAFS spectra can be well represented as a simple linear combination of the Zn foil EXAFS and the Zn K-edge EXAFS spectrum for the as-prepared (Zn)-N-C (Figure S26 and Table S5, Supporting Information). This suggests that only two species are present in this sample, and that under CO_2RR, only the relative concentrations of these species change, but not their local structure. LCA results for Zn K-edge XANES and EXAFS are in an excellent agreement, and both suggest that during CO_2RR both at -0.75_{RHE} V and –1.15 V_{RHE}, 50–60% of all Zn species form metallic Zn clusters (**Figure 8**), while the rest of the zinc remains as singly dispersed metal sites. After the reaction, Zn species return to the original +2 oxidation state with ca. 90% of the Zn now forming singly dispersed sites, and ca. 10% of the Zn remaining as metallic clusters (at least immediately after the reaction). This is in accordance with the findings from TEM imaging, as we observed some crystalline particles (Figure S9, Supporting Information) after CO_2RR at –1.15 V_{RHE}. It is important to note that the results presented in Figure 8 do not represent thermodynamic data. In fact, they simply reflect the ratio of different metal-containing species (i.e., single-atoms/ oxides versus zero-valent metallic states) after 1 hour of electrolysis, and these might not necessarily be the thermodynamically stable phases at the respective potentials. Thus, these states are determined by the kinetics of cluster formation or the kinetics of the reduction of metal-oxides to metallic phases.

For Cu-N-C, we obtained good *operando* XANES fits using as standards the reference spectrum for the as-prepared Cu-N-C, the spectrum for the Cu foil and the spectrum for small Cu_{64} nanoparticles.[75] Including the spectrum for bulk Cu_2O was also considered, but did not lead to any improvement of the fit. We note here that the spectrum for small Cu NPs differs from the spectrum for bulk Cu both due to the reduced Cu coordination numbers, but also due to the reduced Cu-Cu interatomic distances in the small clusters.[75] We furthermore note that if the contribution of small Cu clusters is not explicitly included, LCA results in a wrong conclusion about the presence of significant amounts of Cu(I) species, an artifact of the LCA procedure that has been repeatedly reported in the literature.[76,77] The LCA-XANES results for Cu-N-C, summarized in Table S5 (Supporting Information), suggest that the majority of Cu species are converted to the metallic state under CO_2RR conditions, with only ca. 7% of Cu remaining in form of cationic species at –0.55 V_{RHE}, and only ca. 1% at –1.15 V (Figure 8). After reduction, when plac-

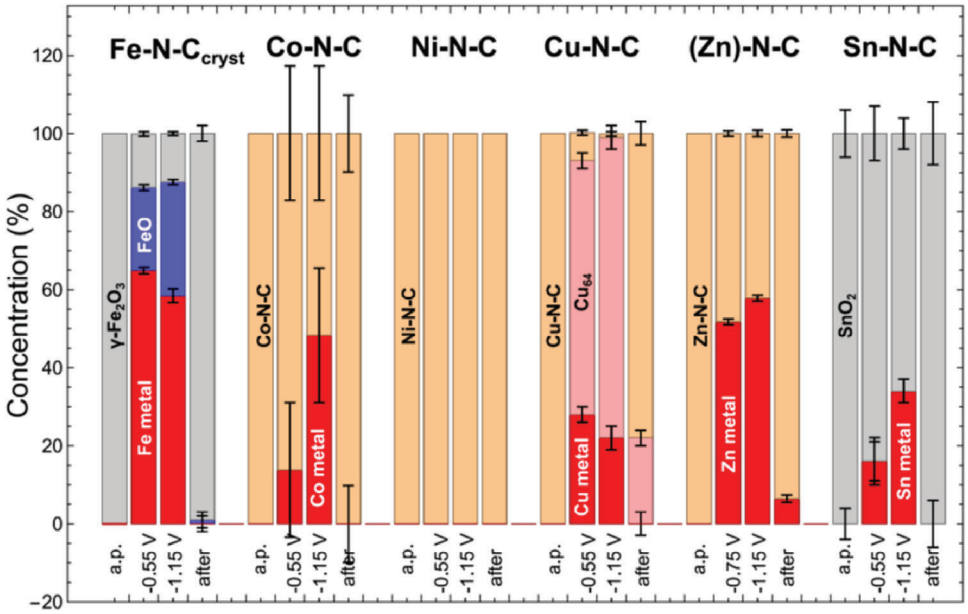

Figure 8. Speciation of M-N-C catalysts in the as prepared state, during CO_2RR at potentials indicated in the plot, and when exposed to air after CO_2RR at −1.15 V_{RHE}. The concentrations of metallic and cationic species were obtained in LCA-XANES analysis, except for Co-N-C, where instead we relied on EXAFS fits, and the concentration of cationic Co species was obtained as Co-O coordination number, divided by 6 (the Co-O/N/C coordination number in as-prepared Co-N-C).

ing the catalyst in air again, most of the clusters returned to the singly-dispersed state (+2 oxidation state) characteristic of the as-prepared catalyst, in accordance with previous reports.[43,44,46,47] The relative weights of Cu_{64} and Cu foil spectra in the *operando* Cu K-edge XANES data collected at these two potential values, in turn, can provide insight into the particle sizes. Indeed, at both potentials the weight of the Cu_{64} spectrum is higher than the weight of the Cu foil, suggesting that the Cu clusters in our samples are just slightly larger than the sub-nanometer-sized Cu_{64} clusters. However, at –0.55 V_{RHE} the weight of the Cu_{64} standard is about 2 times higher than the weight of the Cu foil spectrum, while at –1.15 V_{RHE} it is about 3 times higher, suggesting that the average particle sizes are smaller in the latter case. We hypothesize that the different potential values affect the kinetics of cluster formation. The slower, more gradual cluster formation at less negative potentials result in the formation of thermodynamically more favorable larger clusters. At more negative potentials, the conversion of Cu single sites into Cu clusters is faster, but the system remains trapped in a metastable state due to the reduced mobility of these quickly formed metallic Cu particles.

For Fe-N-C_{cryst} and Sn-N-C samples, which in the as-prepared samples are dominated by oxide clusters, LCA-XANES analysis (Figures S25 and S29, Supporting Information) implies a gradual reduction of cationic Fe species. First, Fe^{3+} (or Sn^{4+}) species are reduced to the + 2 state (Figure S29, Supporting Information), followed by the slower formation of metallic species. For Fe-N-C_{cryst}, both at –0.55 and –1.15 V potential, ≈60% of the Fe species are present in the form of metallic clusters. The formation of metallic clusters is completely reversible, and no metallic Fe is detected in the sample after the reaction. Interestingly, at the more negative potential (−1.15 V_{RHE}) we observed a slightly higher proportion of FeO, compared to the −0.55 V case, which is counterintuitive from a purely thermodynamic point of view, as metallic Fe is the stable phase at these negative potentials. It has to be noted, however, that multiple parallel processes take place in the studied potential window: the reduction of singly dispersed cationic species / metal oxide clusters, the CO_2RR and the HER takes place in parallel. On one hand, the higher reaction rate for CO_2RR/HER at −1.15 V_{RHE} is expected to result in an increased local pH at the catalyst surface, which shifts the stability region of the oxide species to more negative values. At more negative potentials, the kinetics of CO_2RR/HER might also be favored compared to the Fe_2O_3→FeO→Fe transition. Due to these factors, more iron species might end up "trapped" in the FeO state at −1.15 V_{RHE} than at

−0.55 V_{RHE} in the investigated timeframe. At longer times, however, we would expect that the Fe-N-C_{cryst} catalyst will be dominated by metallic Fe at both potentials, as dictated by the thermodynamic equilibriums. Our results, in fact, unveil the presence and relevance of metastable species and phases during electrocatalysis, which might be kinetically stabilized under CO_2RR.

Observing Figure S29 (Supporting Information), one can see that especially for Fe-N-C_{cryst} the 1 h of CO_2RR is not sufficient to reach the final state of the catalyst at −1.15 V_{RHE}. Both, at −0.55 V_{RHE} and at −1.15 V_{RHE}, the transformation of Fe^{3+} into Fe^{2+} is very quick, followed by a much slower transformation of Fe^{2+} into metallic Fe. While at −0.55 V the latter transformation is faster, it seems that the final concentration of metallic Fe species stabilizes at ca. 60%. For −1.15 V_{RHE}, in turn, while after 1 h the concentration of metallic Fe is slightly lower, from Figure S29 (Supporting Information) one can project that the concentration of metallic Fe will further increase after longer CO_2RR times the concentration of metallic Fe in this sample will exceed that in the same sample at −0.55 V_{RHE}.

For Sn-N-C, all *operando* XANES spectra could be represented as linear combinations of spectra for bulk SnO_2, and metallic Sn with only a minor contribution of Sn^{2+} species. In agreement with the results of visual examination of the EXAFS spectra, we observe that a more negative potential results in a more pronounced formation of metallic Sn species (34% of Sn is in a metallic state at –1.15 V, in comparison to only 16% at –0.55 V). Thus, the LCA-XANES seems to validate our previous EXAFS-based conclusions about the presence of metallic Sn in working Sn-N-C catalysts. We also note that the reduction of SnO_2 to metallic Sn is kinetically slower that the reduction of Fe_2O_3, as most of the tin remains in the SnO_2 state even at $-1.15\ V_{RHE}$.

One should note, however, that both in the interpretation of Sn K-edge XANES and Fe K-edge XANES due to the lack of suitable reference spectra for well-defined subnanometer metallic clusters, we neglected the possible effect of particle sizes on XANES spectra (which, as mentioned above, were important for a correct Cu K-edge XANES interpretation). Furthermore, here we neglected the possibility that the local structure around the remaining cationic species can change significantly under CO_2RR conditions: the latter effect, and associated changes in XANES spectra, resulted in our inability to use LCA-XANES for the analysis of Ni-N-C and Co-N-C samples. Similar changes in the local structure could affect also cationic Fe and Sn species, thus, the obtained results, especially those regarding the amounts of Fe^{2+} and Sn^{2+} species present in these samples, should be treated with caution. Therefore, XANES data analysis needs to be considered only together with the insight from EXAFS data.

Results of EXAFS data fitting are presented in Figures S27 and S28 and Table S6 (Supporting Information). The employed EXAFS fitting model and the detailed discussion of EXAFS fitting results are provided in Note S1 (Supporting Information). EXAFS fitting demonstrates that the local structure parameters match those for bulk reference oxides in the case of Fe-N-C_{cryst} and Sn-N-C (γ-Fe_2O_3 and SnO_2), thus confirming once again the presence of oxide clusters in these samples. For the other *as prepared* M-N-Cs, EXAFS fitting suggests an octahedral coordination with a large structural disorder, and average interatomic distances deviating from the values of respective bulk reference oxides. These results thus agree with those obtained by us for the Ni-N-C system,[31] and allow us to speculate that in all these systems, similarly as in Ni-N-C, the M-N_4 structural motifs (in addition to axial M-O bonds), play a prominent role. For spectra collected during CO_2RR, EXAFS fitting confirms the emergence of metal-metal contribution in Fe-N-C_{cryst}, Co-N-C, Cu-N-C, and (Zn)-N-C catalysts. For the Fe-N-C_{cryst}, Cu-N-C, and (Zn)-N-C the metal-metal coordination numbers are practically the same at –0.55 V (–0.75 V for (Zn)-N-C) as at –1.15 V, in agreement with LCA-XANES analysis results. In contrast to these cases, for Co-N-C (and also for Sn-N-C) we observe significant enhancement of the metallic M-M contribution at more negative potentials, suggesting that the kinetics of cluster formation is significantly faster at the more negative potentials.

Another important observation from the EXAFS data fits is the evolution of the single site species (coexisting with emerging metallic clusters) under CO_2RR conditions. One can note that a common feature of Fe-N-C_{cryst}, Co-N-C, Ni-N-C, and Sn-N-C catalysts is that the first shell distance between the metal and its nearest (non-metallic) neighbor noticeably and reversibly contracts under CO_2RR conditions: for Ni-N-C it changes from ≈1.96 Å to 1.88 Å, for Co-N-C form ≈2.06 Å to ≈1.91 Å, for Fe-N-C it decreases from 1.97 Å to 1.91 Å, for Sn-N-C from 2.05 Å to ≈2.01 Å. In the case of Fe-N-C_{cryst} and Sn-N-C these changes are especially remarkable, considering that the reduction of Fe^{3+} and Sn^{4+} species to Fe^{2+} and Sn^{2+} state should, in fact, result in a significant increase of the M–O bond length, not its contraction. In our previous work on Ni-N-C,[31] we have demonstrated that such a contraction is a consequence of the interactions between the single metal site and CO adsorbates. Thus, our interpretation of this contraction of the 1st coordination shell distance differs from that proposed in Ref,[50] which was attributed to nickel hydroxide formation. As is clear from our STFT results, no oxide or hydroxide clusters are present in our Ni-N-C, Cu-N-C, Co-N-C, or (Zn)-N-C catalysts. Instead, the observed contraction of the average interatomic distance is a direct result of exchanging the axial M-O bonds with shorter M-CO bonds, and is an evidence that such interactions are present in all these M-N-C materials. In this context, it is important to notice that for (Zn)-N-C, the contraction of the first shell interatomic distance is much less pronounced (it decreases from ≈2.03 to ≈2.00 Å). We believe that this result can be correlated with much lower degree of CO_2 conversion observed for the bare (Zn)-N-C catalyst than for other M-N-C catalysts that we investigated.

We note that the details of sample preparation, such as the chosen value of annealing temperature might have a significant impact on the formation of clusters in the M-N-C catalysts.[78] While the systematic discussion of the sample preparation is outside the scope of this work, we note that at least for our Ni-N-C catalysts the exact annealing temperature (700 vs 800°C in this example) only had a minor impact on the catalyst's structure and the corresponding XAS spectra in as-prepared state and under CO_2RR conditions (Figure S30, Supporting Information).

2.4. Discussion

The similar response of the M-O bond to the CO_2RR conditions, revealed for all our M-N-C catalysts by detailed EXAFS analysis, demonstrates the universal behavior of these materials. The metals in the studied M-N-C catalysts are in a + oxidation state in the as prepared samples (either as singly dispersed cations or oxide species), become reduced to a metallic state during CO_2RR (with Ni-N-C catalyst being an important exception), and finally almost totally reversibly oxidize back to their original state. Despite the obvious differences between our samples based on different transition metals (most visible being the presence of small SnO_2 and γ-Fe_2O_3 structures already in the *as prepared* Sn-N-C and Fe-N-C catalysts) we render it probable that in all these cases, the singly dispersed species that coexist with oxide and metallic clusters, play a prominent role in the catalytic functionality. Indeed, our TEM and XPS results suggest that in all our as-prepared samples, including those where the oxide clusters were observed, dispersed metal sites, and bonds between them and N-functional groups in the carbon support can be clearly detected. The reversible transformations of the local structure around these species during CO_2RR, as revealed by XANES and EXAFS, in turn, suggest that these single sites can actively inter-

act with CO adsorbates, thus directly participating in the reaction mechanisms.

Our study also suggests that the reversible formation of metallic clusters under CO_2RR conditions is a more common feature of the M-N-C catalysts than previously presumed, being not just a peculiarity of Cu-based M-N-C catalysts, the only material system so far for which such effect was demonstrated. While the reversible reduction of the small Fe and Sn oxide clusters under negative applied potential, observed in our work, is not particularly surprising, we show that singly dispersed Co and Zn species in M-N-C catalysts tend to form metallic clusters too. As in the case of Cu, also for Co and Zn the intriguing feature of this transformation is its reversibility. Namely, when exposed to air after CO_2RR, instead of just getting oxidized and forming oxide clusters, most of the metallic Cu, Co and Zn particles formed during CO_2RR are completely destroyed, and the metal species become redispersed as single sites. This XAS result is in a good agreement with the post reaction TEM analysis, where we could not observe the presence nanoparticles for these samples (except some rare Zn-rich agglomerates). In the context of ZIF-8 derived M-N-C materials, the reversible behavior of the residual Zn from the framework (our (Zn)-N-C sample) observed in our work, is particularly noteworthy. Indeed, the residual Zn species are present in all our samples, since Zn is the part of the precursor. Thus, under CO_2RR conditions, there are always some metallic Zn particles present. Considering that metallic Zn is a good catalyst for CO_2 conversion to CO itself, the role of these Zn species always needs to be carefully considered, when discussing the properties of ZIF-8 derived M-N-Cs. While the formation of metallic Zn particles was reported before, this effect was dismissed as minor.[50] In contrast, our present study shows that up to 60% of Zn species can form metallic Zn clusters during CO_2RR, thus, the total loading of metallic Zn clusters can be comparable to the loading of the secondary metal considered as most active. It is also important to note that even though we observed the reversible cluster formation phenomena for Cu-N-C during CO_2RR, our catalyst did not produce any significant amounts of C_{2+} products. In contrast, we observed high selectivity for HER with minor amounts of CO, indicating that the presence of metallic clusters alone is not sufficient for C_{2+} product formation.[37,46] We envision that the Cu-content, cluster size, properties of the carbon support (e.g., morphology, hydrophobicity, N-content), the strength of the metal-support interaction and the catalyst microenvironment act together in defining the selectivity of Cu single site catalysts, as reported earlier.[79] We hypothesize that the Cu clusters formed under our reaction conditions are still too small to favor C-C coupling as indicated in a prior work with Cu NPs larger than 5 nm being required to obtain significant yields of hydrocarbon products.[45] Indeed, our XAS analysis results suggest that the average size of the Cu clusters in our sample is well below 2 nm. The studies on Cu-N-C catalysts suggest that particle size is a critical parameter for determining the C_{2+} selectivity[79] and in this regard there is full agreement between a size-dependency of CO_2RR selectivities for Cu particles derived from Cu-N-C catalysts, and the observations for Cu particles prepared by other methods.[37,45] All these studies suggest that particles that are less than 10 nm in size are not producing C_{2+} products in significant quantities, which we confirm here.

Considering that the formation of metallic clusters is observed in Fe, Sn, Co, Cu, and Zn species, the fact that no metallic clusters are formed in Ni-N-C catalyst is particularly interesting. The observed reversible changes in XANES and EXAFS spectra for Ni-N-C catalysts are thus solely due to the distortion of the Ni-N_4 structural motif and changes in the local coordination. We emphasize here that the local structure transformations involving Ni single sites, are similar to those involving single metal sites in our other M-N-C catalysts coexisting with metallic clusters. Here, we raise the question, what is the driving force for this dynamic behavior (i.e., cluster formation and redispersion) for certain metals and which factors determine whether it takes place for a specific metal site? One might expect that a higher density of single metal sites in the precatalyst sample might result in a higher probability of cluster formation. We observed, however, that the metallic cluster formation during CO_2RR is not directly correlated with that: the Ni-content in Ni-N-C (0.13 at%) is higher than the Cu content in Cu-N- C (0.08%), nevertheless, cluster were formed for Cu-N-C, but not for Ni-N-C. This suggests that the coordination environment of the metal sites plays a determining role.

A possible explanation can be given considering the differences in metal-support interactions and, in particular, the metal-nitrogen binding energies. Based on our EXAFS results, we conclude that in all our catalysts the local environment of the single metal site involves M-N bonds with the support, coexisting with axial M-O bonds. In the case of Ni-N-C, the Ni-N bond seem to be stronger than the Ni-O, as suggested by the significantly shorter interatomic distance in the first coordination shell in the as-prepared Ni-N-C catalyst in comparison to Ni-O bond in oxide reference. For the other M-N-Cs, in turn, the interactions with oxygen seem to dominate, potentially leading to higher mobility of the metal species during CO_2RR, and, consequently, to formation of metallic clusters. The excellent stability of the Ni-N_4 single sites is also manifested in their outstanding CO_2 to CO conversion performance. However, as mentioned above, the M-N_4 structural motifs for other M-N-Cs, while less stable than Ni-N_4 motifs, still can play an important role in the activity and selectivity obtained. This is supported by the fact that a significant fraction of the metal species in other M-N-Cs also preserve their singly dispersed nature during CO_2RR, and that the clusters formed redisperse in an oxidizing environment. Indeed, both of these observations support a previous assumption that there may be M atoms that bond to both, the N-C support and the formed metallic clusters, leading to restricted particle growths and reversibility.[50] Regarding the mechanism behind the reversible cluster formation in M-N-C catalysts we note that even for the most studied case of Cu-N-C catalysts, no consensus has yet been reached in the literature on the origin of the redispersion effect observed after reaction. Nonetheless, interactions between the clusters formed under working conditions with the N-C support or with the electrolyte have been proposed as key contributors behind the redispersion effect.[48,80] In particular, Weng et al proposed that small oxide clusters are thermodynamically unstable on N-C supports, which was used to explain why the redispersion of the clusters is preferred over their oxidation.[48] In this regard the formation and redispersion of metal clusters on N-C supports during electrocatalytic CO_2RR could have an analogous origin to the reversible exsolution of metal nanoparticles from doped perovskites, known

to take place in thermal catalysis when cycling between reductive and oxidating conditions.[81–83]

The potential-dependencies (or the lack of thereof) of XANES and EXAFS spectra provide further possibilities for correlating the spectroscopic results with the catalytic functionality. Here we note that the potential independent behavior of Fe-N-C_{cryst}, as observed by XAS (within error bars), is in accordance with the observation that the CO-formation rate only marginally increased with the increasing overpotential. The active sites for CO_2RR are already formed at –0.55 V_{RHE}, and their amount does not grow at more negative potentials. In addition, they exhibit slow kinetics toward CO_2RR in the studied potential range, thus, HER starts to dominate at more negative potentials. Even though from these results we cannot tell unambiguously whether the active species for CO_2 reduction are the formed metallic, remaining oxide nanoparticles, or the singly dispersed iron sites, the potential-dependence of the FE and partial current density for CO, however, are in a good agreement with previous studies suggesting Fe single atoms as the active sites.[68]

In contrast, for Co-N-C and Sn-N-C, the obtained XAS spectra depend strongly on the applied potential, which we mostly interpreted as a result of enhanced metallic cluster formation at more negative potentials. It is plausible that the selectivity shift toward HER at the most negative studied potential can be linked to this effect in the case of Co-N-C. Similarly, the larger amount of metallic Sn at increasingly negative potentials could explain the higher formate selectivity and production rate under more reducing conditions. In the latter case, we envision that the *operando* formed metallic Sn clusters coexisting with the SnO_x and even minority Sn single atom species jointly constitute the active sites for CO_2 to formate production.[84,85]

3. Conclusion

With this detailed systematic operando spectroscopic work, we were able to give interesting insights into the evolution of the structure of metal-nitrogen doped carbon catalysts during CO_2RR, filling a gap in the literature on these promising catalyst materials. We showed that the working state of these materials is extremely complex and even when starting from a well-defined system, such as our Co-N-C or Cu-N-C catalyst containing exclusively single atomic metal sites in the *as prepared* state, the coexistence of single atomic sites and metallic cluster/nanoparticles during reaction complicates the experimental diagnosis of the active sites for CO_2RR. As we demonstrated in this work, the in situ formation of metallic cluster/nanoparticles from single atoms during CO_2RR is not unique for Cu, but happens for Zn and Co sites too. Thus, these metallic species can also contribute the CO_2 reduction performance in addition to the remaining singly-dispersed cationic sites. The exact understanding of the mechanism of this phenomenon, however, will require further *operando* analysis on well-defined model catalysts prepared by advanced synthesis methods, complemented with theoretical calculations and modeling.

4. Experimental Section

Synthesis of the Catalysts: The metal-nitrogen doped carbon (M-N-C) catalysts were synthesized by an impregnation-calcination method[54] see Scheme 1. We chose this two-step synthesis method (instead of incorporating the metals during the carbonization process) to separate the N-C formation from the metal-doping. This is expected to result in a more uniform catalyst structure, with most of the metals located at the surface, and not trapped by the carbon shell.[54,86] Thus, the nitrogen-doped carbon support (N-C) was first prepared by the carbonization of a zeolitic-imidazolate framework (ZIF-8) precursor. In a typical synthesis, 4.24 g $Zn(NO_3)_2 \cdot 6H_2O$ (98%, Acros Organics) and 4.92 g 2-methylimidazole ($C_4H_6N_2$, 99% Sigma-Aldrich) were dissolved in 500 mL methanol, heated to 60°C and stirred for 24 hours under reflux. The obtained ZIF-8 powder was collected by centrifugation, washed thoroughly with methanol (2×) and ethanol (1×), and dried at 60 °C in air. Next, it was pyrolyzed in a tube-furnace in Ar flow (200 mL min^{-1}) at 1000 °C for 1 h. The heating rate was 5 °C min^{-1}. At 1000 °C, most of the coordinated Zn reduced to the metallic state and evaporated (boiling point of Zn is 907 °C), leaving behind a porous N-doped carbon structure.[21] The obtained N-C was subjected to acid washing for 24 h, using excess amount of 20 w% HNO_3 (HNO_3, ≥ 65%, Carl Roth) at room temperature, to remove the remaining crystalline Zn-phases. Finally, the sample was washed thoroughly with ultrapure water, until close to neutral pH was reached.

To synthesize the M-N-C catalysts, 200 mg N-C was dispersed in 20 mL solution containing the respective metal ion (6 mM) in isopropanol (C_3H_7OH, ≥ 99.8%, Sigma-Aldrich). The used metal-salts were as follows: $Ni(NO_3)_2 \cdot 6H_2O$ (Sigma-Aldrich, 99.999%), $Cu(NO_3)_2 \cdot 3H_2O$ (Sigma-Aldrich, > 99%), $Co(NO_3)_2 \cdot 6H_2O$ (Sigma-Aldrich, ≥ 98%), $Fe(NO_3)_3 \cdot 9H_2O$ (Sigma-Aldrich, ≥ 98%) and $SnCl_2 \cdot 2H_2O$ (Alfa Aesar, > 98%). The suspensions were sonicated for 2 hours at ≈40°C in an ultrasonic bath, then stirred with a magnetic stirrer at room temperature for another 2 h. The respective metal-impregnated N-C ("M-N-C precursor") was collected by centrifugation, dried at 60°C in air and heat-treated in Ar flow (200 mL min^{-1}) at 700°C for 1 h. The final Ni-N-C and Co-N-C catalysts were obtained after thorough washing with ultrapure water and drying. In the cases of Cu-N-C and Sn-N-C and Fe-N-C, XRD / TEM analysis revealed the presence of crystalline phases after the last washing step, therefore, another acid washing step was necessary. Cu-N-C was stirred in 20 w% HNO_3 for 24 h, while in the case of Sn-N-C, a 6 w% HNO_3 solution was used. Fe-N-C was thoroughly washed first with 0.5 M HNO_3, then with 0.5 M HCl. Finally, the catalysts were washed with ultrapure water until close to neutral pH of the supernatant solution was reached.

For comparison, the "metal-free" (Zn)-N-C catalyst was also included in this study. It is important to note, however, that all samples involving the bare (Zn)-N-C, contain Zn, which remained in the carbon structure despite the multiple heat-treatments and acid leaching steps.

Electrode Preparation: For the electrochemical measurements, the catalysts were spray-coated onto a preheated (≈90 °C) carbon-paper supports (Freudenberg H15C13). The catalyst ink consisted of 40 mg M-N-C powder, 100 µL Nafion 117 solution (5%, Sigma-Aldrich), 3.2 mL isopropanol and 3.2 mL ultrapure water. The catalyst loading was 1.3 ± 0.1 mg cm^{-2}.

Electron Microscopy (EM): Images were acquired using a probe-corrected JEM-ARM 200F (JEOL, Japan) scanning transmission electron microscope (STEM) equipped with a cold field emission gun (CFEG) operated at 200 kV. The high angle annular darkfield (HAADF), annular brightfield (ABF), and brightfield (BF) detector signals were collected from an electron probe with a 14.2 mrad convergence semi-angle and a 90–370, 12–40, 18 mrad collection semi-angle, respectively. The beam current was kept at 11 pA and its resulting electron dose was scaled by the pixel size. Image acquisition and manipulation was performed with DigitalMicrograph software v2.4 (Gatan, USA).

Energy-dispersive X-ray Spectroscopy (EDS) spectra and elemental mapping were acquired using a Talos F200X (ThermoFisher Scientific, USA) STEM operated at 200 kV and equipped with four silicon drift detectors (SDDs). The 72 pA electron beam with a 10.5 mrad probe convergence semi-angle was scanned across the region of interest under a continuous frame acquisition mode. The EDS quantification was performed using the Velox software v1.4.2 (ThermoFisher Scientific, USA). To reduce the background signal of the carbon framework, the net (baseline intensity counts removed) elemental maps are displayed to highlight the presence of the doping heavy metals.

For the post CO_2RR TEM analysis the M-N-C catalysts were deposited onto glassy carbon electrodes to avoid the presence of the carbon originating eventually from the carbon paper, which may be mistaken for the catalyst itself. After performing CO_2RR on these electrodes at –1.15 V potential for 80 minutes, we removed the catalysts from the glassy carbon plates by sonication in pure ethanol.

X-ray Diffraction (XRD): X-ray diffractograms were recorded on a Bruker D8 Advance instrument in powder mode with a Cu anode (8046.3 eV) between 10° and 90° (2Θ). The step size was 0.02° and the dwell time was 3 s.

Inductively Coupled Plasma mass Spectrometry (ICP-MS): Catalysts were first digested in a microwave digestion system (Anton Paar, Multiwave GO) at 180 °C for 20 min in an acid-mixture containing cc. HNO_3, cc. H_2SO_4, cc. HCl in volume ratio of 2:2:6. Then, the solutions were filtered and diluted to ≈50 mL with ultrapure water. For the ICP-MS measurement a 20x dilution of each sample in 3% HNO_3 was prepared. The measurements were performed with a ThermoScientific iCAP RQ instrument.

X-ray Photoelectron Spectroscopy (XPS): XPS spectra were acquired on a SPECS spectrometer with Al Kα source (300 W, 12.52 kV). Survey spectra were acquired with 100 eV pass energy, 0.1 s dwell time, 0.75 eV step size and 2 scans. The N1s and the metal 2p regions were recorded with 30 eV pass energy, 0.3 s dwell time, 0.15 eV step size and 20 and 60 scans, respectively. Data analysis and fitting were performed in the CasaXPS Software. High resolution spectra were fitted with 70% Gaussian – 30% Lorentzian line shape and a Shirley background was applied. The binding energy scale was adjusted assigning the signal of graphitic carbon to 285 eV. The FWHM for N peaks was fixed between 1.5 and 1.6, and the spectra were fitted based on previously established protocols for similar materials.[59,61–63]

X-Ray Absorption Spectroscopy (XAS): X-ray absorption spectroscopy (XAS) measurements were carried out at CLAESS beamline of ALBA synchrotron radiation facility (Barcelona, Spain) at the K-edges of Fe (7112 eV), Co (7709 eV), Ni (8333 eV), Cu (8979 eV) and Zn (9659 eV). Sn K-edge data (29200 eV) for Sn-N-C catalyst were collected at SOLEIL beamline of SAMBA synchrotron (Saint-Aubin, France). All data for the M-N-C catalysts were collected in fluorescence mode, using an energy-selective 6-channel Si drift detector (ALBA) or 32-channel Ge detector (SOLEIL). A Si(311) monochromator (at ALBA) or Si(220) monochromator (at SOLEIL) were used for energy selection.

For *operando* XAS measurements, the samples were mounted in the home-built single compartment electrochemical cell.[31] Samples were spray-coated on carbon paper that acted both as a working electrode and as a window for the X-ray fluorescence and incoming X-rays. As a counter electrode, a Pt mesh was used. A leak-free Ag/AgCl electrode was used as a potential reference. Continuous flow of the electrolyte – CO_2-saturated 0.1 M $KHCO_3$ – was ensured by a peristaltic pump. The potential was controlled by a *BioLogic* potentiostat. Alignment, background subtraction and normalization of the collected XAS data were performed using the *Athena* software.[87] Fitting of the extended X-ray absorption fine structure (EXAFS) spectra was performed using the FEFFIT code.[87] Details and results of the EXAFS data fitting are provided in Supplementary Note 1. Short time Fourier analysis of the EXAFS spectra and linear combination analysis of XANES and EXAFS spectra were performed using home-built *Wolfram Mathematica* scripts.

Electrochemistry Measurements and Product Detection: The electrochemical measurements were performed using an Autolab PGSTAT302N potentiostat / galvanostat. The working electrode was the catalyst-coated carbon paper usually with 0.5–1 cm^2 geometric surface area. The counter electrode was a platinum-mesh and potentials were measured against a leak-free Ag/AgCl electrode, having 0.242 V potential versus SHE. The potentials are reported throughout the text, unless otherwise stated, versus the reversible hydrogen electrode (RHE), calculated using the following equation: E (vs RHE) = E (vs Ag / AgCl) + 0.242 V + 0.059·pH. The solution resistance (R_u) for the IR correction was determined by electrochemical impedance spectroscopy using the high frequency intercept of the semicircle on the Nyquist plot with the real axis. The IR-corrected potential (E_{-IR}) was calculated with the following formula $E_{-IR} = E - I \cdot R_u$, where E is the applied / measured potential, while I is the applied / measured current.

Double layer capacitance (C_{DL}) of the M-N-C electrodes was determined by measuring cyclic voltammograms with different scan rates in a potential region where no faradaic reactions take place. C_{DL} was determined by plotting the difference of the measured current during the anodic and cathodic half-cycle, respectively, versus the scan rate. Roughness factors were calculated by normalizing the C_{DL} value of the respective M-N-C electrode by the C_{DL} of the (Zn)-N-C reference.

CO_2 reduction experiments were carried out in a gas-tight two-compartment H-type cell. The cathode and anode compartments were separated by a Selemion anion exchange membrane to avoid product mixing. CO_2 was continuously bubbled through the anolyte and catholyte with 20 mL min^{-1} flow-rate. The electrolysis was performed in a CO_2-saturated 0.1 M potassium bicarbonate ($KHCO_3$, 99%, Alfa Aesar) solution pretreated with an ion-exchange resin (Chelex 100 Resin sodium form; Bio-Rad) to remove the incidental metal contaminants. The gas outlet of the cathode compartment was directly connected to the injector of the gas-chromatograph via a 6-port-valve, allowing online detection of the gaseous products. Samples were automatically injected in every 15 min of the reaction.

Gas products were detected and quantified by an Agilent 7890B gas chromatograph. The products were separated by different columns (Molecular sieve 13X, HayeSep Q, and Carboxen-1010 PLOT) and subsequently quantified with a flame ionization detector (FID) as well as a thermal conductivity detector (TCD).

In the liquid-phase, acetate and formate concentrations were analyzed by a high-performance liquid chromatograph (HPLC, Shimadzu prominence) equipped with a NUCLEOGEL SUGAR 810 column and refractive index detector (RID). Other liquid products (alcohols and aldehydes) were quantified with a liquid GC (L-GC, Shimadzu 2010 plus) equipped with a fused silica capillary column and flame ionization detector.

The Faradaic efficiencies (FE) of the gas products were calculated using the following equations

$$I_{i,partial} = V_i \cdot f \cdot \frac{n_i \cdot F \cdot p_0}{RT_0} \quad (1)$$

$$FE\ (\%) = \frac{I_{partial}}{I_{total}} \cdot 100\% \quad (2)$$

where Viis the volume concentration of gas products obtained from a previous calibration of the gas chromatograph; f is the volumetric flow-rate of the gas stream leaving the cathode compartment of the cell measured by an universal flow meter (ADM 100, Agilent Technologies); n_i is the number of transferred electrons for a certain product; I_{total} is the total current density measured during electrolysis at the time of injection into the gas chromatograph;$I_{partial}$ is the partial current density of a certain product; F is the Faraday constant (96485 C mol^{-1}); R is universal gas constant (8.314 J mol^{-1} K^{-1}); T_0: temperature (273.15 K); p_0 is the pressure (101 325 Pa);

The Faradaic efficiencies of the liquid products were detected at the end of the electrolysis, therefore after accumulation throughout the measurement time

$$FE_{i,liq}\ (\%) = \frac{c_i * V_{el} * F * n_i}{Q_{total}} \cdot 100\% \quad (3)$$

where V_{el} is the volume of the electrolyte; $c_{i\ \text{is the concentration of prodct i,}}$ Q_{total} is the total charge passed throughout the electrolysis.

For the calculation of the FE values for gas products, the current values were used at the time of the gas sampling. The product composition at that time, however, reflects the catalytic activity of a slightly earlier time (delay time due to the relatively large headspace volume), which were not taken into account. This, together with the error of the gas chromatographic analysis can cause slight deviations of the ΣFE from 100%.

Supporting Information

Supporting Information is available from the Wiley Online Library or from the author.

Acknowledgements

D.H. thanks the funding provided by the Alexander von Humboldt Foundation. Additional funding from the Deutsche Forschungsgemeinschaft (DFG, German Research Foundation) – project no. 406944504 – SPP 2080 and Germany´s Excellence Strategy – EXC 2008 – 390540038 – UniSysCat is greatly appreciated. XAS experiments were performed at CLAESS beamline at ALBA synchrotron with the collaboration of ALBA staff. The authors also acknowledge SOLEIL for provision of synchrotron radiation facilities and we would like to thank beamline staff for assistance in using the beamline "SAMBA." The authors thank Dr. Stefanie Kühl, Walter Wachsmann for their help with the ICP-MS measurements, and Dr. Bernd Steinhauer for the technical support during the experimental work.

Open access funding enabled and organized by Projekt DEAL.

Conflict of Interest

The authors declare no conflict of interest.

Data Availability Statement

The data that support the findings of this study are available from the corresponding author upon reasonable request.

Keywords

active sites, cluster formation, CO_2 conversion, operando XAS, Single atom catalysts

Received: August 3, 2023
Revised: November 9, 2023
Published online: December 7, 2023

[1] P. D. Luna, C. Hahn, D. Higgins, S. A. Jaffer, T. F. Jaramillo, E. H. Sargent, *Science* **2019**, *364*, eaav3506.
[2] A. A. Samu, A. Kormányos, E. Kecsenovity, N. Szilágyi, B. Endrodi, C. Janáky, *ACS Energy Lett.* **2022**, *7*, 1859.
[3] F. Franco, C. Rettenmaier, H. S. Jeon, B. Roldan Cuenya, *Chem. Soc. Rev.* **2020**, *49*, 6884.
[4] B. Endrodi, G. Bencsik, F. Darvas, R. Jones, K. Rajeshwar, C. Janáky, *Prog. Energy Combust. Sci.* **2017**, *62*, 133.
[5] S. Nitopi, E. Bertheussen, S. B. Scott, X. Liu, A. K. Engstfeld, S. Horch, B. Seger, I. E. L. Stephens, K. Chan, C. Hahn, J. K. Nørskov, T. F. Jaramillo, Ib Chorkendorff, *Chem. Rev.* **2019**, *119*, 7610.
[6] Y. Chen, S. Ji, C. Chen, Q. Peng, D. Wang, Y. Li, *Joule* **2018**, *2*, 1242.
[7] M. Li, H. Wang, W. Luo, P. C. Sherrell, J. Chen, J. Yang, *Adv. Mater.* **2020**, *32*, 2001848.
[8] C. D. Dinh, T. Burdyny, G. Kibria, A. Seifitokaldani, C. C. M. Gabardo, F. P. G. Arquer, A. Kiani, J. P. Edwards, P. D. Luna, O. S. Bushuyev, C. Zou, R.-Q. Bermudez, Y. Pang, D. Sinton, E. H. Sargent, *Science* **2018**, *360*, 783.
[9] W. Ma, S. Xie, T. Liu, Q. Fan, J. Ye, F. Sun, Z. Jiang, Q. Zhang, J. Cheng, Y. Wang, *Nat. Catal.* **2020**, *3*, 478.
[10] B. Endrodi, E. Kecsenovity, A. Samu, T. Halmágyi, S. Rojas-Carbonell, L. Wang, Y. Yan, C. Janáky, *Energy Environ. Sci.* **2020**, *13*, 4098.
[11] S. Mitchell, J. Pérez-Ramírez, *Nat. Commun.* **2020**, *11*, 4302.
[12] R. Jasinski, *Nature* **1964**, *201*, 1212.
[13] G. Wu, K. L. More, C. M. Johnston, P. Zelenay, *Science* **2011**, *332*, 443.
[14] W. Ju, A. Bagger, G.-P. Hao, A. S. Varela, I. Sinev, V. Bon, B. Roldan Cuenya, S. Kaskel, J. Rossmeisl, P. Strasser, *Nat. Commun.* **2017**, *8*, 944.
[15] D. Gao, T. Liu, G. Wang, X. Bao, *ACS Energy Lett.* **2021**, *6*, 713.
[16] Z.-L. Wang, X.-F. Hao, Z. Jiang, X.-P. Sun, D. Xu, J. Wang, H.-X. Zhong, F.-L. Meng, X.-B. Zhang, *J. Am. Chem. Soc.* **2015**, *137*, 15070.
[17] A. Roy, D. Hursán, K. Artyushkova, P. Atanassov, C. Janáky, A. Serov, *Appl. Catal. B* **2018**, *232*, 512.
[18] A. S. Varela, N. Ranjbar Sahraie, J. Steinberg, W. Ju, H.-S. Oh, P. Strasser, *Angew. Chem., Int. Ed.* **2015**, *54*, 10758.
[19] F. Pan, W. Deng, C. Justiniano, Y. Li, *Appl. Catal. B* **2018**, *226*, 463.
[20] G. Jun, H. Chia-Shuo, B. Lichen, C. H. Ming, H. Xile, *Science* **2019**, *364*, 1091.
[21] N. Mohd Adli, W. Shan, S. Hwang, W. Samarakoon, S. Karakalos, Yi Li, D. A. Cullen, D. Su, Z. Feng, G. Wang, G. Wu, *Angew. Chem., Int. Ed.* **2021**, *60*, 1022.
[22] Z. Chen, X. Zhang, W. Liu, M. Jiao, K. Mou, X. Zhang, L. Liu, *Energy Environ. Sci.* **2021**, *22*, 2349.
[23] T. Möller, W. Ju, A. Bagger, X. Wang, F. Luo, T. Ngo Thanh, A. S. Varela, J. Rossmeisl, P. Strasser, *Energy Environ. Sci.* **2019**, *12*, 640.
[24] D. M. Koshy, A. T. Landers, D. A. Cullen, A. V. Ievlev, H. M. Meyer, C. Hahn, Z. Bao, T. F. Jaramillo, *Adv. Energy Mater.* **2020**, *10*, 2001836.
[25] X.-M. Hu, H. H. Hval, E. T. Bjerglund, K. J. Dalgaard, M. R. Madsen, M.-M. Pohl, E. Welter, P. Lamagni, K. B. Buhl, M. Bremholm, M. Beller, S. U. Pedersen, T. Skrydstrup, K. Daasbjerg, *ACS Catal.* **2018**, *8*, 6255.
[26] A. S. Varela, M. Kroschel, N. D. Leonard, W. Ju, J. Steinberg, A. Bagger, J. Rossmeisl, P. Strasser, *ACS Energy Lett.* **2018**, *3*, 812.
[27] S. Liang, L. Huang, Y. Gao, Q. Wang, B. Liu, *Adv. Sci.* **2021**, *8*, 2102886.
[28] P. Su, K. Iwase, S. Nakanishi, K. Hashimoto, K. Kamiya, *Small* **2016**, *12*, 6083.
[29] C. F. Wen, F. Mao, Y. Liu, X Y. Zhang, H. Q. Fu, L. R. Zheng, P. F. Liu, H. G. Yang, *ACS Catal.* **2020**, *10*, 1086.
[30] S. Liu, H. B. Yang, S-Fu Hung, J. Ding, W. Cai, L. Liu, J. Gao, X. Li, X. Ren, Z. Kuang, Y. Huang, T. Zhang, B. Liu, *Angew. Chemie Int. Ed.* **2020**, *59*, 798.
[31] A. Martini, D. Hursán, J. Timoshenko, M. Rüscher, F. Haase, C. Rettenmaier, E. Ortega, A. Etxebarria, B. Roldan Cuenya, *J. Am. Chem. Soc.* **2023**, *31*, 17351.
[32] X. Wang, Z. Chen, X. Zhao, T. Yao, W. Chen, R. You, C. Zhao, G. Wu, J. Wang, W. Huang, J. Yang, X. Hong, S. Wei, Y. Wu, Y. Li, *Angew. Chem.* **2018**, *130*, 1962.
[33] Y. Pan, R. Lin, Y. Chen, S. Liu, W. Zhu, X. Cao, W. Chen, K. Wu, W.-C. Cheong, Yu Wang, L. Zheng, J. Luo, Y. Lin, Y. Liu, C. Liu, J. Li, Qi Lu, X. Chen, D. Wang, Q. Peng, C. Chen, Y. Li, *J. Am. Chem. Soc.* **2018**, *140*, 4218.
[34] D. Hursán, A. A. Samu, L. Janovák, K. Artyushkova, T. Asset, P. Atanassov, C. Janáky, *Joule* **2019**, *3*, 1719.
[35] D. Wang, X. Li, J. Yang, J. Wang, D. Geng, R. Li, M. Cai, T.-K. Sham, X. Sun, *Phys. Chem. Chem. Phys.* **2013**, *15*, 3535.
[36] J. Li, P. Prslja, T. Shinagawa, A. J. Martín Fernández, F. Krumeich, K. Artyushkova, P. Atanassov, A. Zitolo, Y. Zhou, R. García-Muelas, N. López, J. Pérez-Ramírez, F. Jaouen, *ACS Catal.* **2019**, *9*, 10426.
[37] W. Rong, H. Zou, W. Zang, S. Xi, S. Wei, B. Long, J. Hu, Y. Ji, L. Duan, *Angew. Chem., Int. Ed.* **2021**, *60*, 466.
[38] S. Chen, Y. Li, Z. Bu, F. Yang, J. Luo, Q. An, Z. Zeng, J. Wang, S. Deng, *J. Mater. Chem. A* **2021**, *9*, 1705.
[39] C. Xu, X. Zhi, A. Vasileff, D. Wang, Bo Jin, Y. Jiao, Y. Zheng, S.-Z. Qiao, *Small Struct.* **2021**, *2*, 2000058.

[40] T. Zhang, S. Verma, S. Kim, T. T. Fister, P. J. A. Kenis, A. A. Gewirth, *J. Electroanal. Chem.* **2020**, *875*, 113862.
[41] H. Yang, Yu Wu, G. Li, Q. Lin, Qi Hu, Q. Zhang, J. Liu, C. He, *J. Am. Chem. Soc.* **2019**, *141*, 12717.
[42] K. Zhao, X. Nie, H. Wang, S. Chen, X. Quan, H. Yu, W. Choi, G. Zhang, B. Kim, J. G. Chen, *Nat. Commun.* **2020**, *11*, 2455.
[43] H. Xu, D. Rebollar, H. He, L. Chong, Y. Liu, C. Liu, C.-J. Sun, T. Li, J. V. Muntean, R. E. Winans, Di-J Liu, T. Xu, *Nat. Energy* **2020**, *5*, 623.
[44] L. Ma, W. Hu, B. Mei, H. Liu, B. Yuan, J. Zang, T. Chen, L. Zou, Z. Zou, Bo Yang, Yi Yu, J. Ma, Z. Jiang, Ke Wen, H. Yang, *ACS Catal.* **2020**, *10*, 4534.
[45] R. Reske, H. Mistry, F. Behafarid, B. Roldan Cuenya, P. Strasser, *J. Am. Chem. Soc.* **2014**, *136*, 6978.
[46] C. E. Creissen, M. Fontecave, *Nat. Commun.* **2022**, *13*, 2280.
[47] D. Karapinar, N. T. Huan, N. Ranjbar Sahraie, J. Li, D. Wakerley, N. Touati, S. Zanna, D. Taverna, L. H. Galvão Tizei, A. Zitolo, F. Jaouen, V. Mougel, M. Fontecave, *Angew. Chem., Int. Ed.* **2019**, *58*, 15098.
[48] Z. Weng, Y. Wu, M. Wang, J. Jiang, K. Yang, S. Huo, X.-F. Wang, Q. Ma, G. W. Brudvig, V. S. Batista, Y. Liang, Z. Feng, H. Wang, *Nat. Commun.* **2018**, *9*, 415.
[49] J. Timoshenko, B. Roldan Cuenya, *Chem. Rev.* **2021**, *121*, 882.
[50] J. Li, A. Zitolo, F. A. Garcés-Pineda, T. Asset, M. Kodali, P. Tang, J. Arbiol, J. R. Galán-Mascarós, P. Atanassov, I. V. Zenyuk, M. T. Sougrati, F. Jaouen, *ACS Catal.* **2021**, *11*, 10028.
[51] X. Li, Y. Zeng, C.-W. Tung, Y.-R. Lu, S. Baskaran, S-Fu Hung, S. Wang, C.-Q. Xu, J. Wang, T.-S. Chan, H. M. Chen, J. Jiang, Qi Yu, Y. Huang, J. Li, T. Zhang, B. Liu, *ACS Catal.* **2021**, *11*, 7292.
[52] Y. Zeng, J. Zhao, S. Wang, X. Ren, Y. Tan, Y.-R. Lu, S. Xi, J. Wang, F. Jaouen, X. Li, Y. Huang, T. Zhang, B. Liu, *J. Am. Chem. Soc.* **2023**, *145*, 15600.
[53] Y. Deng, J. Zhao, S. Wang, R. Chen, J. Ding, H.-J. Tsai, W.-J. Zeng, S.-Fu Hung, W. Xu, J. Wang, F. Jaouen, X. Li, Y. Huang, B. Liu, *J. Am. Chem. Soc.* **2023**, *145*, 7242.
[54] J. Li, H. Zhang, W. Samarakoon, W. Shan, D. A. Cullen, S. Karakalos, M. Chen, D. Gu, K. L. More, G. Wang, Z. Feng, Z. Wang, G. Wu, *Angew. Chem., Int. Ed.* **2019**, *58*, 18971.
[55] J. Cravillon, S. Münzer, S.-J. Lohmeier, A. Feldhoff, K. Huber, M. Wiebcke, *Chem. Mater.* **2009**, *21*, 1410.
[56] C. H. Choi, C. Baldizzone, G. Polymeros, E. Pizzutilo, O. Kasian, A. K. Schuppert, N. Ranjbar Sahraie, M.-T. Sougrati, K. J. J. Mayrhofer, F. Jaouen, *ACS Catal.* **2016**, *6*, 3136.
[57] M. C. Biesinger, B. P. Payne, A. P. Grosvenor, L. W. M. Lau, A. R. Gerson, R. S. C. Smart, *Appl. Surf. Sci.* **2011**, *257*, 2717.
[58] S. Muralidharan, R. G. Hayes, *J. Chem. Phys.* **1979**, *71*, 2970.
[59] K. Artyushkova, *J. Vac. Sci. Technol. A* **2020**, *38*, 31002.
[60] K. Friedel Ortega, R. Arrigo, B. Frank, R. Schlögl, A. Trunschke, *Chem. Mater.* **2016**, *28*, 6826.
[61] S. Ott, F. Du, M. L. Luna, T. A. Dao, S. Selve, B. R. Cuenya, A. Orfanidi, P. Strasser, *Appl. Catal. B* **2022**, *306*, 121118.
[62] I. Matanovic, K. Artyushkova, M. B. Strand, M. J. Dzara, S. Pylypenko, P. Atanassov, *J. Phys. Chem. C* **2016**, *120*, 29225.
[63] F. Späth, W. Zhao, C. Gleichweit, K. Gotterbarm, U. Bauer, O. Höfert, H.-P. Steinrück, C. Papp, *Surf. Sci.* **2015**, *634*, 89.
[64] C. E. Nanayakkara, P. M. Jayaweera, G. Rubasinghege, J. Baltrusaitis, V. H. Grassian, *J. Phys. Chem. A* **2014**, *118*, 158.
[65] M. C. Biesinger, L. W. M. Lau, A. R. Gerson, R. S. C. Smart, *Appl. Surf. Sci.* **2010**, *257*, 887.
[66] F. Luo, A. Roy, L. Silvioli, D. A. Cullen, A. Zitolo, M. T. Sougrati, I. C. Oguz, T. Mineva, D. Teschner, S. Wagner, Ju Wen, F. Dionigi, U. I. Kramm, J. Rossmeisl, F. Jaouen, P. Strasser, *Nat. Mater.* **2020**, *19*, 1215.
[67] NIST X-ray Photoelectron Spectroscopy Database, https://srdata.nist.gov/xps/EngElmSrchQuery, aspx?EType=PE&CSOpt=Retri_ex_dat&Elm=Sn, **2000**.
[68] T. N. Huan, N. Ranjbar, G. Rousse, M. Sougrati, A. Zitolo, V. Mougel, F. Jaouen, M. Fontecave, *ACS Catal.* **2017**, *7*, 1520.
[69] C. Genovese, M. E. Schuster, E. K. Gibson, D. Gianolio, V. Posligua, R. Grau-Crespo, G. Cibin, P. P. Wells, D. Garai, V. Solokha, S. Krick Calderon, J. J. Velasco-Velez, C. Ampelli, S. Perathoner, G. Held, G. Centi, R. Arrigo, *Nat. Commun.* **2018**, *9*, 935.
[70] S. Li, S. Zhao, X. Lu, M. Ceccato, X.-M. Hu, A. Roldan, J. Catalano, M. Liu, T. Skrydstrup, K. Daasbjerg, *Angew. Chem., Int. Ed.* **2021**, *60*, 22826.
[71] L. Han, S. Song, M. Liu, S. Yao, Z. Liang, H. Cheng, Z. Ren, W. Liu, R. Lin, G. Qi, X. Liu, Q. Wu, J. Luo, H. L. Xin, *J. Am. Chem. Soc.* **2020**, *142*, 12563.
[72] J. Timoshenko, A. Kuzmin, *Comput. Phys. Commun.* **2009**, *180*, 920.
[73] M. Muñoz, P. Argoul, F. Farges, *Am. Miner.* **2003**, *88*, 694.
[74] S. Xiang, P. Huang, J. Li, Y. Liu, N. Marcella, P. K. Routh, G. Li, A. I. Frenkel, *Phys. Chem. Chem. Phys.* **2022**, *24*, 5116.
[75] S. V. Myers, A. I. Frenkel, R. M. Crooks, *Chem. Mater.* **2009**, *21*, 4824.
[76] A. Halder, C. Lenardi, J. Timoshenko, A. Mravak, B. Yang, L. K. Kolipaka, C. Piazzoni, S. Seifert, V. Bonacic-Koutecký, A. I. Frenkel, P. Milani, S. Vajda, *ACS Catal.* **2021**, *11*, 6210.
[77] W. H. Cassinelli, L. Martins, A. R. Passos, S. H. Pulcinelli, C. V. Santilli, A. Rochet, V. Briois, *Catal. Today* **2014**, *229*, 114.
[78] C. Li, W. Ju, S. Vijay, J. Timoshenko, K. Mou, D. A. Cullen, J. Yang, X. Wang, P. Pachfule, S. Brückner, H. S. Jeon, F. T. Haase, S.-C. Tsang, C. Rettenmaier, K. Chan, B. R. Cuenya, A. Thomas, P. Strasser, *Angew. Chem.* **2022**, *134*, 202114707.
[79] J. Zhang, T. H. My Pham, Z. Gao, M. Li, Y. Ko, L. Lombardo, W. Zhao, W. Luo, A. Züttel, *ACS Catal.* **2023**, *13*, 9326.
[80] E. Boutin, A. Salamé, M. Robert, *Nat. Commun.* **2022**, *13*, 4190.
[81] Y. Nishihata, J. Mizuki, T. Akao, H. Tanaka, M. Uenishi, M. Kimura, T. Okamoto, N. Hamada, *Nature* **2002**, *418*, 164.
[82] K. Kousi, C. Tang, I. S. Metcalfe, D. Neagu, *Small* **2021**, *17*, 2006479.
[83] S. Shah, J. Hong, L. Cruz, S. Wasantwisut, S. R. Bare, K. L. Gilliard-Abdulaziz, *ACS Catal.* **2023**, *13*, 3990.
[84] Y. Zhao, J. Liang, C. Wang, J. Ma, G. G. Wallace, *Adv. Energy Mater.* **2018**, *8*, 1702524.
[85] Y.-W. Choi, F. Scholten, I. Sinev, B. Roldan Cuenya, *J. Am. Chem. Soc.* **2019**, *141*, 5261.
[86] A. Mehmood, M. Gong, F. Jaouen, A. Roy, A. Zitolo, A. Khan, M.-T. Sougrati, M. Primbs, A. M. Bonastre, D. Fongalland, G. Drazic, P. Strasser, A. Kucernak, *Nat. Catal.* **2022**, *5*, 311.
[87] B. Ravel, M. Newville, *J. Sybchrotron Radiat.* **2005**, *12*, 537.